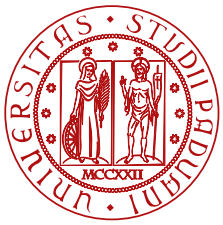

UNIVERSITÀ DEGLI STUDI DI PADOVA

DIPARTIMENTO DI INGEGNERIA DELL'INFORMAZIONE

DIPARTIMENTO DI INGEGNERIA DELL'INFORMAZIONE

CORSO DI LAUREA MAGISTRALE IN BIOINGEGNERIA

Novel non-invasive methodology to map TSPO PET tracers blood-to-brain influx rate

Relatore
Prof. Mattia Veronese

Laureando
Leonardo Barzon

Correlatore
Lucia Maccioni

ANNO ACCADEMICO 2023-2024

Data di laurea 04/09/2024

Ai miei genitori e a chi, come loro, ha sempre creduto in me.

Abstract

Background: Neuroinflammation is a critical feature across various brain disorders, including neurological and neurodegenerative conditions such as multiple sclerosis, Alzheimer's disease, and Parkinson's disease, as well as neuropsychiatric disorders like major depressive disorder and schizophrenia. Positron emission tomography (PET) targeting the 18-kDa translocator protein (TSPO) is the primary tool for in vivo imaging of neuroinflammation. However, significant methodological challenges have limited the development of reliable biomarkers.

Objective: This study aimed to advance non-invasive TSPO PET imaging by using a novel blood-free methodology for estimating the blood-to-brain influx rate constant (K_1). The objective was to validate this approach using the first-generation [^{11}C]-PK11195 and the second-generation [^{11}C]-PBR28 TSPO radiotracers, and to extend it to voxel-level analysis. The primary hypothesis posited that elevated levels of peripheral inflammation would negatively correlate with K_1, indicating reduced delivery of TSPO tracers to the brain.

Methods: A novel non-invasive method utilizing an image-derived input function (IDIF) was employed to estimate the blood-to-brain influx rate constant (K_1) and generate parametric maps. Analyses were conducted at both regional and voxel levels. The method was validated across datasets representing various psychiatric conditions, including major depressive disorder and schizophrenia. Additionally, the impact of peripheral inflammatory markers, body weight and gender on K_1 was systematically assessed.

Results: The methodology was successfully applied to all tracers under investigation and effectively generated meaningful K_1 parametric maps. The study confirmed the hypothesized negative correlation between peripheral inflammation and K_1. Remarkably, the parameter was not influenced by the psychiatric disease. Additionally, significant effects of body weight and gender on K_1 were observed.

Conclusion: This work represents a significant advancement in TSPO PET imaging by providing a reliable, non-invasive method for mapping the blood-to-brain influx of TSPO radiotracers. The study confirms the hypothesis that increased peripheral inflammation is associated with reduced TSPO tracer delivery to the brain and supports the emerging model of peripheral-to-central immune interaction. By accounting for key variables such as body weight, gender,

and peripheral inflammatory status, this research offers crucial insights and improves the potential for biomarker validation in psychiatric disorders. This methodological advancement is pivotal for enhancing the interpretability of TSPO PET measures and advancing the field of neuroinflammation imaging.

List of Figures

List of Tables

List of Acronyms

ACC anterior cingulate cortex.

ANCOVA analysis of covariance.

ANOVA analysis of variance.

BBB blood-brain barrier.

BMI body mass index.

CNS central nervous system.

CRP C-reactive protein.

CSF cerebrospinal fluid.

GM grey matter.

HC healthy controls.

IDIF image-derived input function.

INS insula.

MDD major depressive disorder.

PET positron emission tomography.

PFC prefrontal cortex.

ROI region of interest.

SCZ schizophrenia.

TAC time-activity curve.

TSPO 18 kDa translocator protein.

UHRP ultra high risk of psychosis.

WLLS weighted linear least squares.

WNLLS weighted non-linear least squares.

Contents

Chapter 1

Introduction

Neuroinflammation is a significant pathological hallmark across various brain disorders, ranging from neurological and neurodegenerative conditions such as multiple sclerosis, Alzheimer's disease, and Parkinson's disease, to neuropsychiatric disorders like major depressive disorder and schizophrenia. Positron emission tomography (PET) targeting the 18-kDa translocator protein (TSPO) is currently the primary tool for imaging neuroinflammation in vivo. However, significant methodological challenges have hindered the development of robust biomarkers, which are crucial for the advancement of innovative treatments for brain disorders.

Additionally, current research is exploring the link between peripheral and central immunity, investigating how inflammation in the body can trigger neuroinflammation and ultimately lead to clinical symptoms. In the field of immunopsychiatry, new models of peripheral-to-central inflammation are emerging, emphasizing the critical modulatory role of the blood-brain barrier (Turkheimer et al., 2023). This barrier selectively regulates the passage of solutes from the blood to the brain, playing a crucial role in maintaining brain homeostasis.

In this context, a recently developed non-invasive methodology leverages the full potential of TSPO PET imaging to extract a parameter representing the brain-to-blood influx rate of the radiotracers used to image inflammation (Maccioni et al., 2024). A simplified one-tissue compartmental model, representing the first minutes after tracer injection and approximating the arterial input function with an image-derived input function (IDIF), allows for the straightforward estimation of the microparameter K_1. This novel technology could not only provide unique insights into the regulatory mechanisms of the blood-brain barrier but also be instrumental in assisting TSPO quantification, which has faced significant methodological challenges, particularly in the context of schizophrenia (Marques et al., 2019).

The project aims to expand this innovative non-invasive methodology to new datasets, utilizing both first and second-generation TSPO radiotracers, computing regional blood-to-brain influx rate constants. Furthermore, it seeks to refine the methodology to the voxel-level, uti-

lizing a computationally efficient linear estimation approach. This advancement enables the unique possibility of obtaining parametric maps of the TSPO radiotracers' blood-to-brain influx rate constant. The estimates of K_1 at both the region of interest (ROI) and voxel levels are investigated to identify potential alterations in psychiatric disease or in the presence of peripheral inflammation, as well as the possible influence of demographic and experimental variables.

The hypothesis of this study is to replicate previous findings that have identified an inverse association between the concentration of peripheral inflammatory markers and the influx of tracers from the blood into the brain (Turkheimer et al., 2021). Moreover, this work is expected to extend these findings to the voxel level, utilizing statistical analyses on parametric maps. The results are further elucidated and expanded by imaging transcriptomics analysis, which offers insight into the underlying biological processes involved.

The expected impact of this work is to provide a blood-free, computationally efficient, comprehensive, and generalizable framework capable of mapping the blood-to-brain influx rate of TSPO PET tracers. This tool will enable the acquisition of valuable physiological insights, facilitate the interpretation of TSPO PET signals, and ultimately support research on neuroinflammation biomarkers.

Chapter 2

Background

2.1 Neuroinflammation

2.1.1 Principles of central nervous system inflammation

Neuroinflammation refers to the inflammatory response within the central nervous system (CNS). This process involves the release of various substances, such as cytokines, chemokines, reactive oxygen species, and other second messengers like nitric oxide and prostaglandins. These mediators are produced by resident CNS glial cells, including astrocytes and microglia, endothelial cells, and infiltrating peripheral immune cells (DiSabato et al., 2016).

The effects of neuroinflammation depend on the severity and duration of the initial insult that triggers it. Neuroinflammation is not inherently negative; in fact, microglia play a crucial role in immune surveillance within the brain parenchyma, protecting against injuries and infections (Nimmerjahn et al., 2005). Additionally, neuroinflammatory signaling promotes synaptic plasticity as well as learning and memory (Cornell et al., 2022).

However, unlike beneficial inflammation, severe and chronic neuroinflammation is highly destructive and pathological. It is characterized by significant activation of CNS glia, increased production of cytokines and chemokines, infiltration of peripheral immune cells, edema, and increased permeability and breakdown of the blood-brain barrier (BBB). This is evident in multiple sclerosis (MS), where microglia shift from being protectors to destroyers, leading to demyelination, oligodendrocyte death, and neuroaxonal injury and loss in the CNS (Yong, 2022).

Furthermore, the activation of microglia and astrocytes is implicated in the pathogenesis and progression of other neurodegenerative diseases, such as Alzheimer's disease (AD) and Parkinson's disease (PD) (Kwon & Koh, 2020). In AD, the binding of misfolded and aggregated proteins to receptors on microglia and astroglia triggers an innate immune response that exacerbates disease progression and severity (Heneka et al., 2015). In addition to neurodegenerative

diseases, neuroinflammation has been linked to neuropsychiatric disorders, such as depression and schizophrenia. Further details about these associations will be elucidated in subsequent sections.

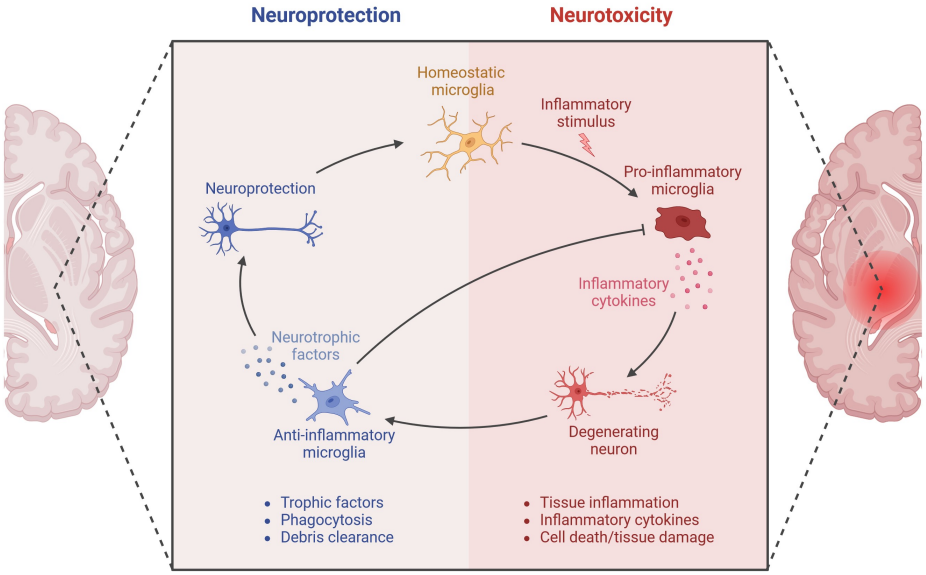

Figure 2.1: Roles of microglia in neuroinflammation: from neuroprotection to neurotoxicity

2.1.2 The blood-brain barrier

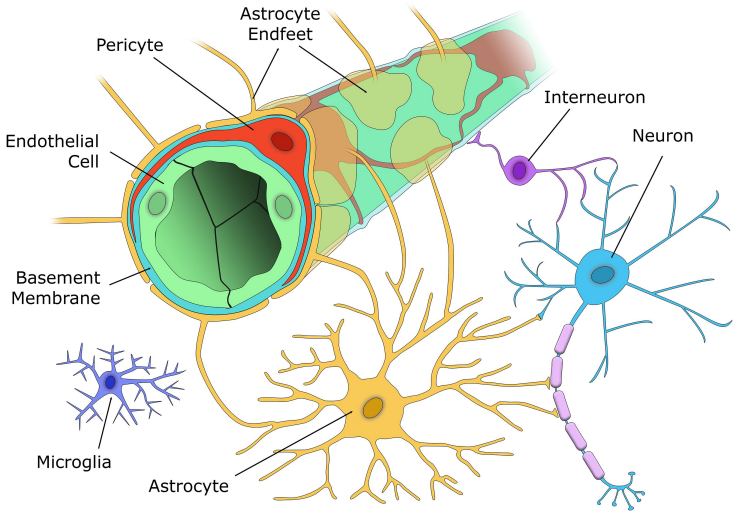

Figure 2.2: Structural components of the blood-brain barrier (BBB)

The blood-brain barrier (BBB) serves as the regulated interface between peripheral blood cir-

culation and the CNS. Anatomically, it constitutes a neurovascular unit primarily composed of cerebral microvascular endothelium, astrocytes, pericytes, neurons, and the extracellular matrix (Fig. 2.2). A complex of transmembrane and cytoplasmic proteins linked to the actin cytoskeleton constitutes the tight junctions between endothelial cells of the BBB (Hawkins & Davis, 2005). The function of this barrier is to restrict paracellular diffusion of hydrophilic substances from the blood to the brain, thereby controlling the influx and efflux of biological substances essential for the brain's metabolic activity and neuronal function. Therefore, the functional and structural integrity of the BBB is crucial to maintaining the homeostasis of the brain microenvironment (Kadry et al., 2020). The BBB is not the only regulated interface between the CNS and the periphery. At the level of the choroid plexus, ependymal cells are joined with tight junctions, forming the blood-CSF barrier (BCSFB). In the retina, the vessels are surrounded by the blood-retinal barrier (BRB) and at the level of the spinal cord by the blood-spinal cord barrier (SCB) (Choi & Kim, 2008)

The mechanisms of solute transfer across the blood-brain barrier are diverse and are graphically summarized in Fig. 2.3. A thorough understanding of these processes is essential for comprehending a broad spectrum of significant biological phenomena. For instance, these barriers are critical for drug delivery to the CNS, presenting significant challenges and serving as targets for emerging strategies, such as nanotechnologies (Nguyen et al., 2021). Additionally, investigating the processes at the BBB level is crucial for elucidating the interplay between peripheral and central immunity. These complex phenomena will be discussed in the context of psychiatric disorders, following the introduction of the primary tool for imaging neuroinflammation in vivo.

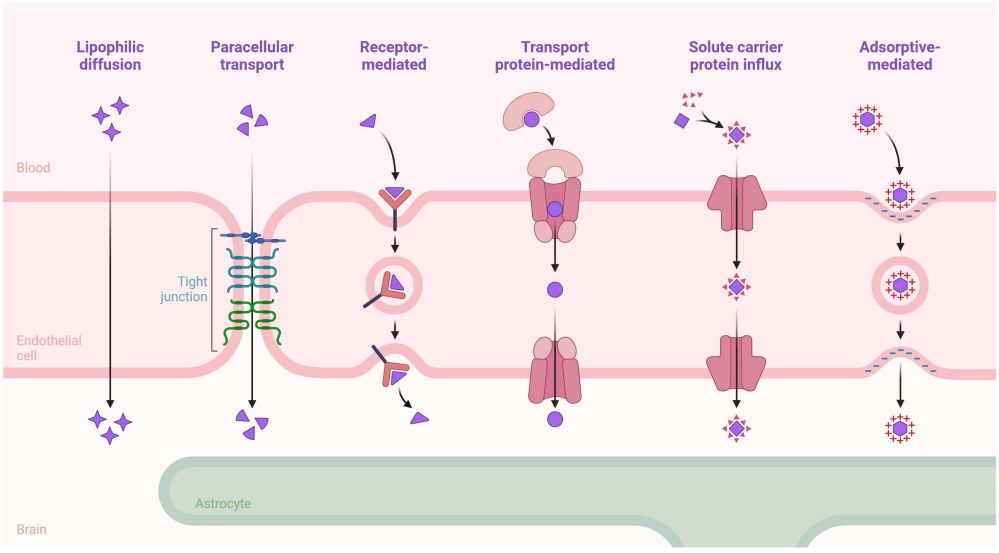

Figure 2.3: Solute transfer across the blood-brain barrier (BBB)

2.2 Neuroinflammatory imaging

2.2.1 Positron emission tomography

Positron emission tomography (PET) is a nuclear medicine technology that allows for the detection of small amounts of radiolabeled compounds, called radiotracers, inside the body (Coura-Filho et al., 2022). A PET tracer is typically derived from natural substances or compounds that interact with specific biochemical processes in the body, such as pharmaceuticals. To accurately follow physiological or biochemical processes, an ideal tracer should possess several specific characteristics (Cherry et al., 2012). First, the tracer's behavior within the organism should closely mimic that of the natural substance. Additionally, the injected mass should be sufficiently small so as not to alter the physiological process being studied, while the tracer's specific activity should be high enough to allow for imaging and blood (or plasma) activity evaluation. Finally, any isotope effect should be negligible. These substances are tagged with short-lived positron-emitting isotopes, such as ^{11}C and ^{18}F, which are produced in a cyclotron. During beta-plus decay, a proton within a radionuclide nucleus is converted into a neutron, releasing a positron and a neutrino. The emitted positron travels a few millimeters in tissue before being annihilated by an electron from the surroundings (Tai & Piccini, 2004). This annihilation event produces two equally energetic photons (511 keV) traveling in opposite directions (180°) along the same line. PET scanners consist of multiple rings of scintillation detectors, which simultaneously capture the photon pairs produced from a single annihilation event, identifying what is known as a coincidence event. The paths followed by each photon pair, referred to as lines of response (LORs), can be traced, and the collected data are used to determine the location of a positron annihilation at a specific time point. Reconstruction software then converts these data into tomographic images.

After injecting a known dose of a radiolabeled compound, expressed in Bq, the concentration of radioactivity within the region or voxels of interest, evaluated in $\mathrm{Bq/ml}$, can be measured. In static scans, primarily used for clinical applications, tracer activity is counted over a single fixed period. In dynamic scans, typically for research purposes, it is measured at multiple time points during an examination lasting approximately 60-90 minutes. The resulting scans can be further analyzed for quantification purposes, i.e., extracting parameters that provide physiological information. Depending on the objective of the PET study, different quantification methods can be employed (Bertoldo et al., 2014).

Static protocols often lead to the computation of semi-quantitative indices, such as the standardized uptake value (SUV), which provides an index of tracer uptake in a region or voxel of interest, normalized to the injected dose of radiotracer and a normalization factor (NF) based on the subject's anthropometric features (e.g., body surface area or body weight):

$$\mathrm{SUV} = \frac{\text{radiotracer concentration}}{\frac{\text{injected dose}}{\text{NF}}} \tag{2.1}$$

The integration of the SUV over a time interval of interest yields the area under the curve (AUC), another commonly used index. Furthermore, through the so-called ratio method, it is possible to estimate the volume of distribution $\mathrm{V_T}$ (ml of plasma/cm^3 of tissue), computed as the ratio at true equilibrium between the tracer concentration in tissue $\mathrm{C_{tissue}}$ ($\mathrm{kBq/cm}^3$) and the tracer concentration in plasma $\mathrm{C_p}$ ($\mathrm{kBq/ml}$). In receptor studies, this method is used to estimate binding potential $\mathrm{BP_{ND}}$ (unitless) by using the concentration of tracer in tissue and in a reference region without specific binding, thus avoiding arterial sampling, which is otherwise needed to obtain $\mathrm{V_T}$.

Transitioning from static to dynamic acquisition protocols allows for the introduction of more informative methodologies. The main techniques in this context are spectral analysis methods, graphical methods, and compartmental modelling. The latter, considered the gold standard for dynamic PET quantification, will be explored in detail as it is crucial for this research work. Compartmental modelling aims to recapitulate the mechanisms of functioning of the investigated biological system and therefore requires a full mathematical description of the system processes. A compartment is defined as a volume within which the tracer rapidly becomes uniformly distributed, such that it exhibits no significant concentration gradients (Cherry et al., 2012). Among the different models proposed in different quantification contexts, the starting reference model for this study is the two-tissue four-parameter model for receptor ligand binding studies (Mintun et al., 1984), depicted in Fig. 2.4.

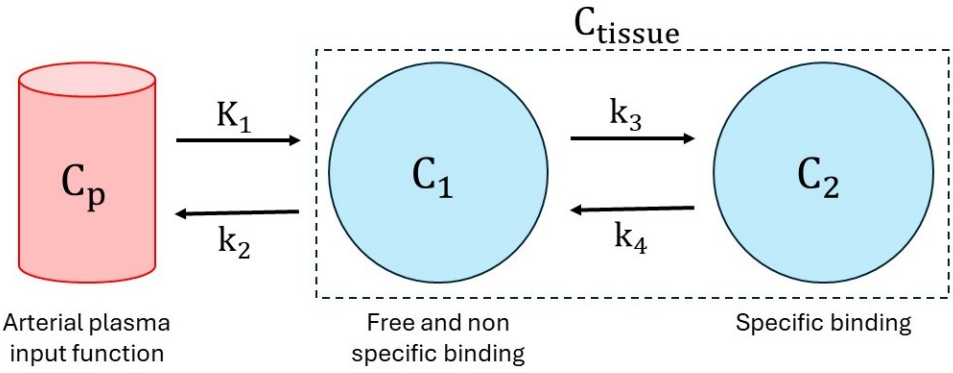

Figure 2.4: Two-tissue four-parameter compartmental model

The first compartment represents the arterial blood pool, with $\mathrm{C_p(t)}$ describing the input function, i.e., the measured tracer concentration in plasma. The other two compartments rep-

resent the kinetic of the radiotracer in the tissue, describing the free and non-specific binding ($C_1(t)$) and the specific binding ($C_2(t)$), respectively. These compartments are connected through the rate constants K_1, k_2, k_3, and k_4, often referred as microparameters. Among these, K_1, denoted with a capital letter, represents the blood-to-tissue influx rate constant and is measured in ml/cm^3/min, while the other parameters are in min^{-1}. From the microparameters, some macroparameters of interest can be derived, e.g., the binding potential (BP_{ND}) or the volume of distribution (V_T).

$$BP_{ND} = \frac{k_3}{k_4}, \qquad V_T = \frac{K_1}{k_2} \cdot \left(1 + \frac{k_3}{k_4}\right). \tag{2.2}$$

The gold-standard procedure for fully identifying the model, i.e., estimating its parameters, necessitates arterial blood sampling throughout the entire duration of the exam. Despite the substantial safety of radial arterial catheterization, with only a few cases of clinical complications (Everett et al., 2009), it can be a source of distress for the patients, potentially discouraging their participation in clinical trials. Furthermore, this procedure adds additional costs to the PET exam: specialized clinical personnel are needed, and the presence of radiometabolites complicates the direct measurement of the parent (unchanged) concentration in plasma, which must be determined using chromatographic techniques (Tonietto et al., 2016).

2.2.2 The methodology of TSPO PET imaging

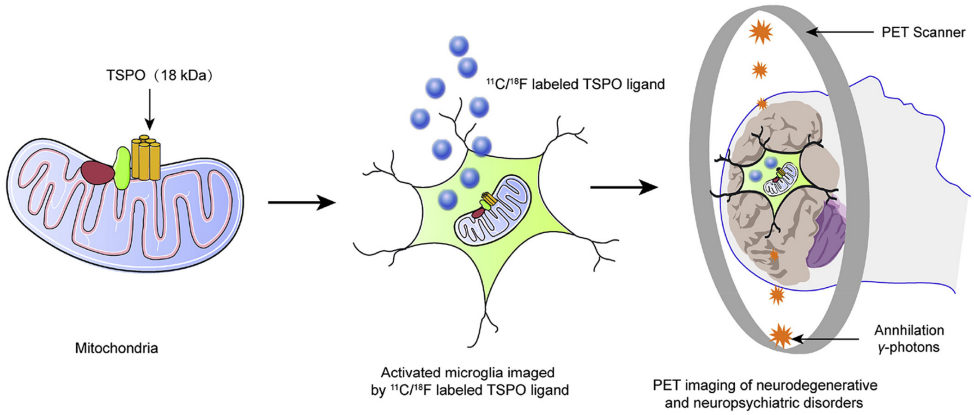

Figure 2.5: TSPO PET imaging in vivo

The 18 kDa translocator protein (TSPO), also referred to as the peripheral benzodiazepine receptor (PBR), is a transmembrane protein situated on the outer membrane of mitochondria. In the CNS, TSPO is highly expressed in glial cells, such as astrocytes and microglia, as well as in

endothelial cells and some populations of neurons (Lee et al., 2020). TSPO is commonly employed as a marker for neuroinflammation or microglia activation, as its expression significantly increases in activated glial cells, particularly microglia, during neural disorders or injury (Kim & Yu, 2015). Consequently, TSPO is a central focus for molecular approaches aimed at imaging neuroinflammation in vivo (Turkheimer et al., 2015). The first developed PET radiotracer enabling TSPO density imaging in the brain is the isoquinoline-carboxamide derivative [^{11}C]-(R)-PK11195, a radiolabeled TSPO antagonist with nanomolar affinity (9.3 nmol). However, quantifying PK11195 data poses several challenges. The first issue is the compound's affinity for multiple binding sites in blood, such as platelets, monocytes, and plasma proteins. Platelets and monocytes have high TSPO densities, which vary with diseases. Normally, the fraction of a radioligand bound to blood cells remains stable at equilibrium but not necessarily at capillaries, where exchanges with tissue occur. Correcting arterial radioactivity by separating blood cells from plasma can be approximate only if the bound fraction is small compared to the free fraction in plasma. This is a problem for PK11195, which has a low free fraction in plasma (about 1-5%), making accurate measurements difficult. Additionally, PK11195 binds to plasma proteins that can be up-regulated during peripheral inflammatory events, which can sometimes accompany brain disorders. If plasma-based quantification is not possible, the time-activity curve (TAC) of a reference brain region can be used instead. However, this method is complicated by the unpredictable location of microglial activation and the widespread presence of TSPO in the brain and blood-brain barrier (BBB).

To overcome these challenges, significant work has been devoted to creating novel radioligands with high affinity for TSPO like [^{18}F]-DPA714 and [^{11}C]-PBR28. These efforts aim to enhance the signal-to-noise ratio compared to PK11195 (Chauveau et al., 2008). However, the anticipated improvements in image quality have not been fully achieved, possibly due to several factors (Turkheimer et al., 2015). First, genetic variations in the TSPO gene, particularly the rs6971 polymorphism, result in different binding affinities among individuals. This variation categorizes people into high-affinity binders (HABs), low-affinity binders (LABs), and mixed-affinity binders (MABs), impacting the interpretation of PET signal. Second, the extremely high affinity of some new ligands can cause a disproportionate signal from TSPO at the BBB compared to brain tissue. This phenomenon occurs because of the high concentration of free ligand near the BBB, masking signals from tissue-bound tracer. Addressing this requires sophisticated kinetic modelling to accurately differentiate these signals (Veronese et al., 2018). Third, challenges in accurately measuring free plasma concentrations persist and pose significant hurdles, as mentioned earlier. Significant research efforts have been made to address the methodological issues of TSPO quantification, including the development of supervised clustering techniques for reference region definition (J. Schubert et al., 2021; Turkheimer et al., 2007).

2.3 Neuroinflammation in neuropsychiatric disorders

This section provides an overview of current research concerning the connection between neuropsychiatric disorders and neuroinflammation, encompassing the rapidly evolving field of immunopsychiatry. It emphasizes the current challenges and the ongoing pursuit of suitable biomarkers, highlighting the critical need for innovative methodologies to shed light on this intricate field, such as the one proposed in this study.

2.3.1 Neuroinflammation in depression

Depression, often referred to as major depressive disorder (MDD), is a prevalent condition which ranks among the top three causes of disability worldwide, impacting approximately 5 % of adults globally (WHO, 2021). Several medications used to treat MDD primarily function by increasing levels of monoamines in the brain. However, treatment efficacy varies widely, and up to one-third of patients do not attain complete relief from symptoms (Rush et al., 2006).

The pressing need for improved treatments has prompted the exploration of new mechanisms for treating MDD, with extensive research into the relationship between neuroinflammation and depression. In this context, inflammatory processes are suggested to play a substantial role in the pathophysiology of major depressive disorder (Bullmore, 2018). Historically, the neuroinflammatory hypothesis of depression has been supported by strong evidence of increased peripheral inflammatory markers in a significant portion of MDD patients (Osimo et al., 2020; Osimo et al., 2019; Pitharouli et al., 2021). The most reliable markers of inflammation in MDD relate to the acute-phase C-reactive protein (CRP) and cytokines of the innate immune response, e.g., TNF-α. Significantly, patients resistant to treatment exhibit notably higher CRP levels, averaging around 5 mg/l (Chamberlain et al., 2019).

Studies utilizing positron emission tomography (PET) with ligands targeting the 18 kDa translocator protein (TSPO) have demonstrated brain microglial activation in response to peripheral immune challenges. For example, high levels of TSPO binding have been observed following acute lipopolysaccharide (LPS) administration, which induces robust peripheral cytokine responses (Peters van Ton et al., 2021). In patients with MDD, TSPO PET imaging has revealed increased microglial activity, although to a lesser extent compared to severe peripheral inflammation models. In previous studies involving MDD cohorts, significantly higher TSPO binding has been observed in the anterior cingulate cortex (ACC) compared to healthy controls (Holmes et al., 2018; Richards et al., 2018; Setiawan et al., 2015, 2018), as well as in the frontal cortex (Holmes et al., 2018; Li et al., 2018; Richards et al., 2018; Setiawan et al., 2015, 2018) and the insula (INS) (Setiawan et al., 2015, 2018). Furthermore, a significant correlation has been found between TSPO binding and depression severity scores in MDD (Setiawan et al.,

2015), as well as a decrease in TSPO binding in MDD patients receiving cognitive behavioral therapy (Li et al., 2018). Additionally, TSPO binding was found to be significantly higher in MDD patients with suicidal thoughts compared to those without (Holmes et al., 2018). A more recent investigation within the Biomarkers in Depression Study (BIODEP) under the NIMA consortium (https://www.neuroimmunology.org.uk/) revealed that TSPO binding, expressed as relative binding potential ($\mathrm{BP_{ND}}$), was significantly elevated in depressed subjects compared to controls, particularly in the ACC, without showing correlations between TSPO PET measures and peripheral inflammatory markers (as indicated by CRP blood levels) or body mass index (BMI) (J. J. Schubert et al., 2021). Moreover, the cited paper offers a comprehensive review of the previously reported case-control differences in TSPO binding studies (Fig. 2.6).

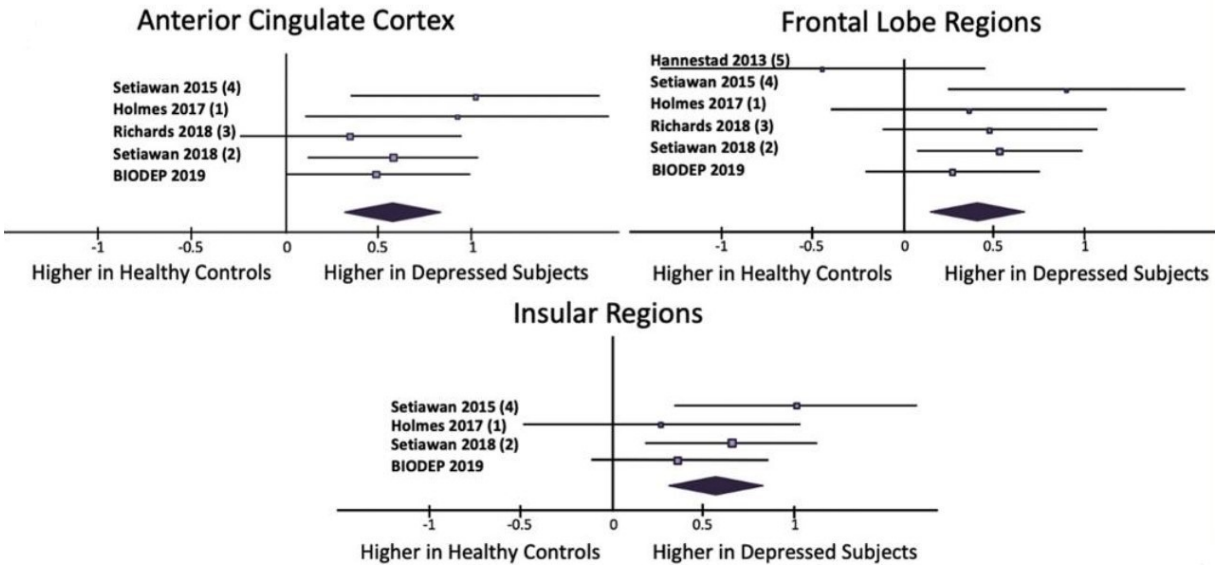

Figure 2.6: Review of TSPO PET studies in depression (J. J. Schubert et al., 2021)

Forest plot summarizing TSPO PET findings from case-control studies of depression in the ACC, frontal lobe, and INS regions.

Importantly, another TSPO PET study observed a marked inverse association between blood-to-CSF exchange measures and peripheral inflammation, as measured by CRP, in healthy subjects and MDD patients of the BIODEP study (Turkheimer et al., 2021). The same study revealed an association between an increase in CRP and a reduction in blood-to-brain tracer percolation in a cohort of seven healthy volunteers, part of the FLAME study (Nettis et al., 2020), after an immune challenge with IFN-α injection. Notably, there was no association of these effects with the marker of BBB leakage, S100β, which remained unchanged.

These recent advancements and new perspectives have led to the development of an inno-

vative model that transcends the conventional view of microglia cells as the primary drivers of depression (Turkheimer et al., 2023). Challenging the traditional understanding of the relationship between peripheral and central immunity in the context of sickness behavior in depression, this theory proposes a more intricate interaction involving peripheral inflammation, blood-brain barrier (BBB) permeability, and central nervous system (CNS) immune responses. The model is applicable to MDD patients who have mild peripheral inflammation (CRP < 10 mg/l), including those who are resistant to traditional antidepressant medications. This new theory, which is graphically schematised in Fig. 2.7, suggests that, in a healthy condition, circulating cytokines are absent or minimal, barrier permeability is normal, and microglial cells remain inactive. Moreover, temporary elevation of circulating cytokines reduces barrier permeability temporarily, disrupting homeostasis and causing mild sickness behavior, while microglial cells remain inactive. Furthermore, with persistent inflammation becoming chronic, structural changes in barrier function occur, leading to depressive behavior accompanied by activated microglia responding to prolonged disturbances in solute concentrations and the BBB. These observations suggest that microglial activity does not directly cause depressive symptoms; rather, it is a consequence of the closure of barriers and subsequent disruption of homeostasis.

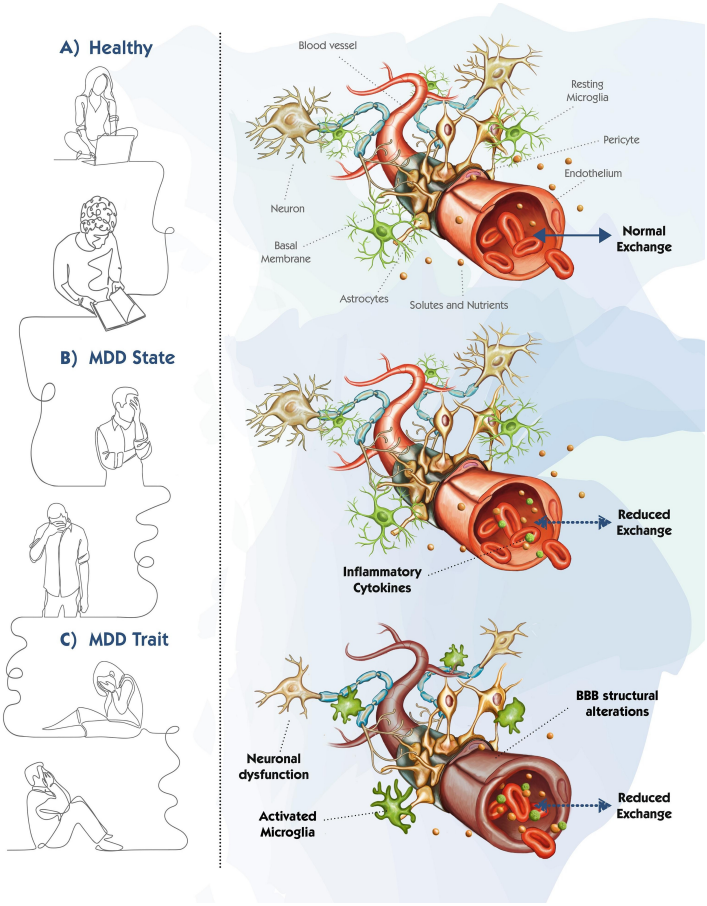

Figure 2.7: A new model of peripheral-central immune interactions (Turkheimer et al., 2023)

2.3.2 Neuroinflammation in schizophrenia

Schizophrenia is marked by psychotic symptoms and often social and occupational decline, posing significant etiological and therapeutic challenges. Affecting about 1% of the population, this condition is slightly more prevalent in men than in women (Jauhar et al., 2022). The exact mechanisms of schizophrenia are not fully understood, and current antipsychotic treatments have significant limitations (Stępnicki et al., 2018). The therapeutic effects of antipsychotics are generally attributed to their interactions with various neurotransmitter receptors. These treatments are effective for only about half of the patients and primarily address positive symptoms like hallucinations and thought disorders, leaving negative symptoms (e.g., flat affect, social withdrawal) and cognitive symptoms (e.g., learning and attention disorders) largely untreated. Additionally, antipsychotics can cause severe neurological and metabolic side effects, such as agranulocytosis in the case of clozapine. Recent research has increasingly linked inflammation to schizophrenia through genetics, epidemiology, and clinical studies. Infection history, autoimmune diseases, and genetic variants in immune-related genes elevate risk (Benros et al., 2011). Additionally, prenatal infections, through maternal inflammatory responses, are linked to schizophrenia and other neurodevelopmental disorders, with studies indicating that maternal immune activation and cytokines like IL-6 play crucial roles (Aguilar-Valles et al., 2020). Furthermore, altered concentrations of peripheral pro-inflammatory cytokines have been reported in schizophrenic patients (Na et al., 2014). Numerous imaging studies have aimed to assess potential alterations in brain microglial activation in patients with schizophrenia spectrum disorders compared to healthy controls, often yielding contradictory findings and inconclusive evidence. A recent meta-analysis by Marques et al. (2019) synthesized findings from TSPO PET studies.

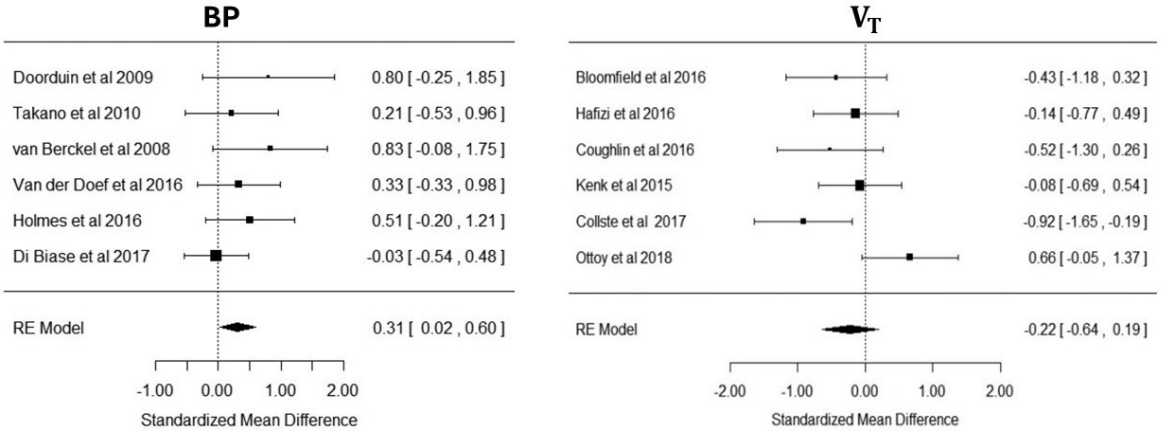

Figure 2.8: Results of meta-analysis on TSPO PET studies in schizophrenia (Marques et al., 2019) Comparison of BP and V_T outcomes between patients with schizophrenia and healthy controls.

The main outcome measured was the difference in TSPO binding, specifically within the total grey matter, quantified by either binding potential (BP) or volume of distribution ($\mathrm{V_T}$). The results, presented in Fig. 2.8, revealed moderate increases in TSPO tracer binding within grey matter in schizophrenia when using BP as an outcome measure, but no significant difference was found when $\mathrm{V_T}$ was used.

However, Plavén-Sigray and Cervenka (2019) criticized this meta-analysis, arguing that BP outcomes with [^{11}C]-PK11195 are unreliable due to low brain uptake and low specific-to-background binding ratios. Additionally, the meta-analysis combined BP measures from different studies, including both binding potential over plasma ($\mathrm{BP_p}$) and non-displaceable binding potential ($\mathrm{BP_{ND}}$), making the results difficult to interpret. Conversely, according to Plavén-Sigray and Cervenka, the conclusions based on $\mathrm{V_T}$ are more reliable as they were derived from studies using second-generation tracers and did not include outcomes expressed relative to tissue, such as distribution volume ratios (DVR), due to the lack of a suitable normalizing region.

In summary, the varied TSPO imaging outcomes likely reflect methodological challenges and prompt questions about accurately interpreting tracer binding in grey matter, warranting further investigation.

Chapter 3

Materials & methods

3.1 Study participants and image acquisition

The data analyzed in this work comprise two datasets, each including TSPO PET imaging data acquired using a different radiotracer. All datasets were made available through a formal collaboration with King's College London.

Dataset 1 consists of 51 subjects diagnosed with major depressive disorder (MDD) and 27 matched healthy controls (HC) (details in Tab 3.1). These data are part of the Biomarkers in Depression Study (BIODEP) under the NIMA consortium (https://www.neuroimmunology.org.uk/), which aims at investigating the role of neuroinflammation in depression. Details on participant enrollment and clinical assessment, as well as information about venous blood sampling for measuring C-reactive protein (CRP) levels, are available in (J. Schubert et al., 2021; Turkheimer et al., 2021). In these previous studies, MDD patients were further stratified based on their blood C-reactive protein (CRP) level, CRP > 3 mg/L corresponding to the high CRP group (n=20) and CRP <= 3mg/L forming the low CRP group (n=31). Notably, one healthy subject lacks CRP assessment. All subjects underwent a 60-minute dynamic PET scan on a GE SIGNA PET/MR scanner (GE Healthcare, Waukesha, USA) following an intravenous bolus injection of [^{11}C]-PK11195 (injected dose 361 $\pm$ 53 MBq). The data were reconstructed using a multi-subject atlas method with enhancements for the MRI brain coil component. Corrections for scatter, random events, and dead time were applied using the GE scanner software. Consistent with best practices for [^{11}C]-PK11195 PET imaging (Turkheimer et al., 2007), no arterial blood data were collected during the PET imaging. During PET data acquisition, each subject also underwent a high-resolution T1-weighted brain MRI scan (BRAVO).

Group	Subjects	Female	Male	Age (years)	Weight (kg)	CRP (mg/l)
HC	27	16	11	37.3 ± 7.8	73.6 ± 14.5	$2.9^* \pm 2.8$
MDD	51	36	15	36.2 ± 7.4	80.3 ± 14.4	1.1 ± 0.9

Table 3.1: Demographic information of subjects included in Dataset 1.

*not considering one missing value

Dataset 2 was part of the data already investigated in (Maccioni et al., 2024). Specifically, King's College London (KCL) provided dynamic [^{11}C]-PBR28 PET and MR images from 94 subjects. The participants included 52 healthy controls (HC), 15 schizophrenia (SCZ) patients, 14 individuals at ultra high risk of psychosis (UHRP), and 13 subjects in the "STRESS" group. The latter participants were healthy individuals exposed to psychosocial risk factors during childhood and adulthood (for further details see Dahoun et al., 2019). Detailed information on the healthy and psychotic subjects, as well as data acquisition protocols, can be found in (Bloomfield et al., 2016). Notably, 7 SCZ patients underwent a second PET scan after administration of XBD173, a drug that selectively binds to the 18 kDa translocator protein, blocking the specific binding signal of the radiotracer (see Marques et al., 2021). Demographic information about all the subjects included in Dataset 2 is reported in Tab. 3.2. In summary, all acquisition protocols began with a low-dose computed tomography (CT) scan for attenuation and scatter correction using a Siemens Biograph TruePoint PET/CT scanner (Siemens Medical Systems, Germany). This was followed by a 90-minute dynamic PET scan after a bolus injection of [^{11}C]-PBR28 (Injected Dose: 327.6 ± 28.5 MBq). The dynamic PET data were reconstructed using filtered back projection with 5 mm isotropic Gaussian smoothing and corrected for random noise, attenuation, and scatter effects. T1-weighted MR brain scan data were collected using a Siemens 3-T MR scanner, either a Siemens Tim Trio or Siemens MAGNETOM Verio.

Group	Subjects	Gender (F/M)	Genotype (HAB/MAB)	Age (y)	Weight (Kg)
HC	52	16/36	32/20	34.0 ± 14.6	74.4 ± 13.9
SCZ	15	3/12	13/2	45.8 ± 10.1	87.5 ± 20.2
UHRP	14	7/7	7/7	24.3 ± 5.4	76.4 ± 13.9
STRESS	13	6/7	11/2	27.7 ± 6.8	72.0 ± 15.6

Table 3.2: Demographic information of subjects included in Dataset 2.

3.2 Methodological framework

In this work, a new non-invasive and simplified methodological framework was utilized for the computation of the blood-to-brain influx rate constant $\mathrm{K_1}$. This parameter, expressed in $\mathrm{ml/cm^3/min}$ represents the rate at which the tracer crosses the blood-brain barrier (BBB) from plasma and, following Fick's law, can be expressed as the product of cerebral blood flow (blood perfusion, F) and the tracer's BBB extraction fraction (E) (Renkin, 1959).

$$\mathrm{K_1 = F \cdot E} \tag{3.1}$$

The extraction fraction (E) is described by the following equation:

$$\mathrm{E = 1 - e^{-\frac{PS}{F}}} \tag{3.2}$$

PS represents the permeability-surface product ($\mathrm{cm^3}$/min/100 g of tissue), which corresponds to the maximum capillary clearance achievable in a capillary bed of specific permeability and surface area.

This method was crafted in a very recent work (Maccioni et al., 2024) and consists of fitting a limited time window of the tracer kinetic after its injection (within 10 minutes), with a simplified model composed by a single irreversible compartment and a non-invasive image-derived input function (IDIF) (1T1K-IDIF). Designed to be completely blood-free, the method relies on three key assumptions, which facilitate further simplification starting from the gold-standard two-tissue compartmental model (Fig. 3.1). First of all, early after injection, exchanges between compartments and venous efflux are minimal, allowing the tracer kinetics to predominantly reflect influx into brain tissue. Consequently, a two-compartment reversible model can be simplified to a single irreversible compartment model. A further simplification involves removing the parameterization of the blood volume fraction ($\mathrm{V_b}$ = 0), resulting in the final linear model for estimating the $\mathrm{K_1}$ parameter (1T1K-$\mathrm{C_p}$). Notably, while assuming $\mathrm{V_b}$ = 0 is standard in brain PET parametric imaging (voxel resolution), it is a significant approximation for region-of-interest (ROI) analysis. Second, shortly after injection, metabolite production from parent radiotracers remains minimal (<10% of the total parent), as observed with many PET tracers (Souza et al., 2021; Tonietto et al., 2016). During this period, assuming an even distribution between red blood cells and plasma is reasonable, making whole blood tracer concentration ($\mathrm{C_b}$) a suitable approximation for parent plasma tracer concentration. This approach uses $\mathrm{C_b}$ as the input function for the model. Third, adopting a robust protocol for extracting IDIF and assuming that computed IDIF closely approximates $\mathrm{C_b}$, it can effectively serve as the input function for the compartmental model (1T1K-IDIF). Therefore, this method offers a blood-sampling-free

alternative for estimating the K_1 parameter.

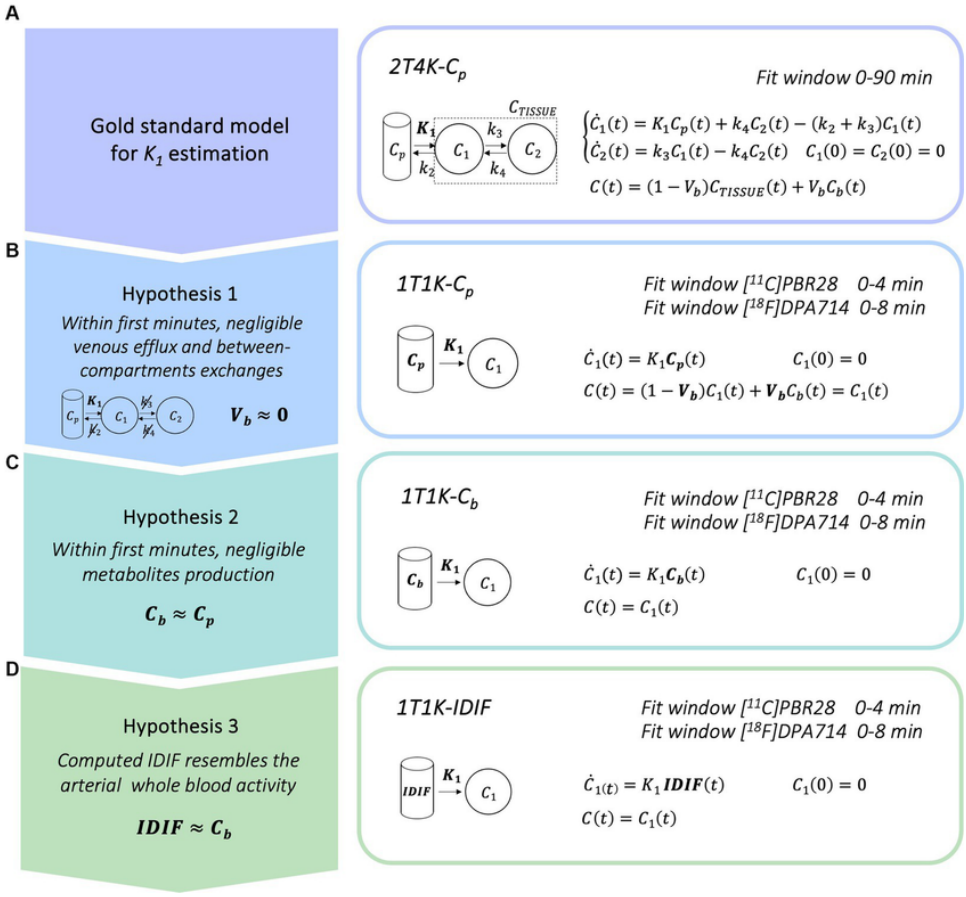

Figure 3.1: Novel blood-free methodological framework for K_1 estimation (Maccioni et al., 2024)

Panel A illustrates the gold standard compartmental model for kinetic modelling of TSPO radiotracers. Panels B, C, and D present the simplified models for K_1 estimation derived by considering a limited time window for model fitting. The reported time intervals were optimized for that previous study, which validated the methodology for the tracers [^{11}C]-PBR28 and [^{18}F]-DPA714.

3.2.1 Data preprocessing and TAC extraction

The provided neuroimaging data had already been pre-processed using different combinations of in-house codes and neuroimaging analysis software, including Statistical Parametric Mapping (SPM, http://www.fil.ion.ucl.ac.uk/spm), FMRIB Software Library (FSL, http://www.fmrib.ox.ac.uk/fsl), and MIAKAT (http://Invicro.org). The pipeline included a step of motion correction of the dynamic PET data, computation of integral PET images, derivation of brain and grey matter masks from structural MR images, performed using FreeSurfer (https://surfer.nmr.mgh.harvard.edu), and registration of brain and tissue masks to the subject's native PET space. Afterwards, the CIC v2.0 neuroanatomical atlas (Tziortzi et al., 2011) was co-registered to each subject's image space. This atlas was masked using a FreeSurfer-derived

mask to isolate voxels belonging to cortical and subcortical regions, excluding white matter and CSF voxels, thus minimizing partial volume effects. The results of this process in a representative subject are shown in Fig. 3.2. Finally, mean regional time-activity curves (TACs) were computed for each subject from the resulting regions of interest (ROIs).

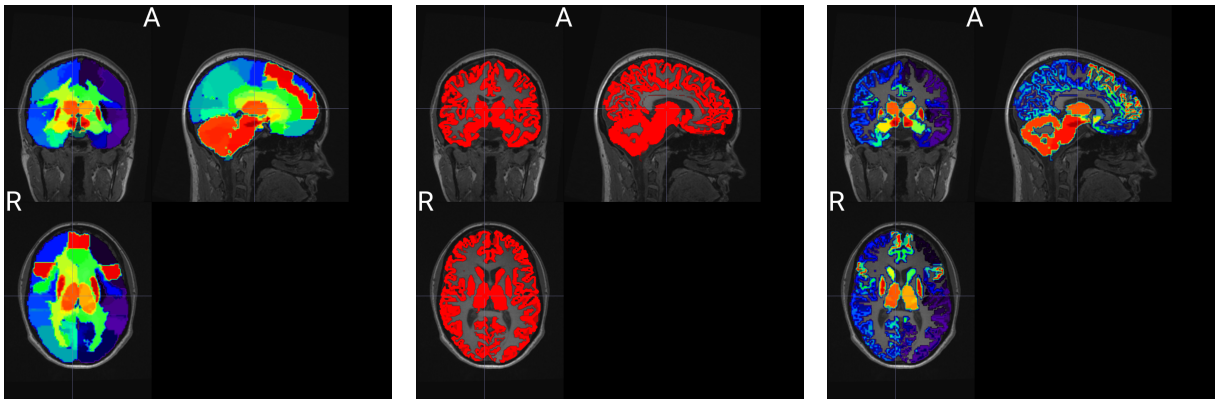

(a) **(b)** **(c)**

Figure 3.2: CIC v2.0 neuroanatomical atlas masking and ROI definition. Results for a representative subject from Dataset 1: (a) ROIs of the CIC v2.0 atlas, (b) FreeSurfer-derived mask, and (c) resulting ROIs after masking.

Unless explicitly specified otherwise, the analyses described below, including kinetic modelling and parameter estimation, were performed using MATLAB R2022a (MathWorks) and encompassed all subjects introduced in Section 3.1.

3.2.2 Image-derived input function (IDIF)

The image-derived input function (IDIF) (Zanotti-Fregonara et al., 2011) is an elegant technique that has emerged to address the limitations of the standard PET input function, which requires the invasive procedure of arterial cannulation (see Section 2.2.1). The IDIF extraction process primarily involves carotid segmentation to obtain raw blood time-activity curves. This segmentation is typically performed using MRI images (Fung et al., 2009) or by placing regions of interest (ROIs) directly on PET images (Mourik et al., 2008). MRI segmentation theoretically offers better carotid identification, but practical implementation is hindered by unreliable coregistration algorithms primarily focused on brain structures above the carotids. This can lead to alignment errors exacerbated by the carotid artery's small, elongated, and flexible nature, influenced by head positioning differences between PET and MRI scans (Zanotti-Fregonara et al., 2011). Conversely, direct PET image segmentation of carotids currently appears more reliable,

avoiding MRI and coregistration issues. Despite challenges in PET image segmentation due to low signal-to-noise ratios, carotid arteries are generally visible in early summed frames post-tracer injection. In recent years, significant progress in PET scanner technology, characterized by enhanced sensitivity, improved spatio-temporal resolution, and extended axial field of view (FOV), has the potential to overcome the challenges associated with IDIF methods (Volpi et al., 2023). These technological advancements, combined with more robust automated techniques, promise to improve the accuracy of measuring blood activity levels, particularly during the crucial early phase, essential for compartmental modelling.

In this work a semi-automated pipeline was utilized to extract the image-derived input function for each dynamical PET scan, in the PET native space, mainly using MATLAB. For Dataset 1, the procedure was applied for the first time in this study, while for Dataset 2, the final extracted IDIFs were already available from previous research (Maccioni et al., 2024). Nevertheless, all the necessary steps are described for all the datasets under investigation. The first step involved arterial carotid siphons segmentation. A preliminary binary mask defining an area including the carotid siphons was already available and obtained by subtracting the individual brain mask with a mask delineating cortical and subcortical regions (Freesurfer "aparc.a2009s+aseg"), using FMRIB Software Library (FSL, version 6.0.3) function *fslmaths*. This initial image was then cropped further to isolate a smaller area containing the siphons. Subsequently, morphological operations were applied to refine this cropped area, aiming to obtain a single connected component. Next, voxels within this refined area were selected based on a lower threshold set to 60% of the maximum peak amplitude in the early dynamic PET frames. Following this, slightly different strategies were applied to the two datasets. For Dataset 2, erosion and dilation operations were performed to remove isolated voxels and delineate the left and right siphons. Conversely, for Dataset 1, the MATLAB function *bwconncomp* was used to extract the two largest connected components representing the carotid siphons. Results for the siphons mask definition are reported in Fig. 3.3. For both datasets, the next step involved computing the correlation between each voxel in the selected area and the dynamics of all other voxels in that region. This step aimed to exclude voxels with highly noisy activities. For Dataset 1, 50% of voxels with the most correlated dynamics were selected, while for Dataset 2, this percentage was set at 70%. Finally, for Dataset 1, an additional selection was made based on voxels with the highest peak amplitude in the early frames, selecting 50 voxels. This step enhances the characterization of the initial peak, which is critical for the methodology. For each scan, the IDIF was obtained by computing the median of the time-activity curves (TACs) of all selected voxels.

Compartmental modelling presumes a noise-free input function. Therefore, the IDIF for each subject was ultimately fitted using a tri-exponential model. This involved applying linear regression to the ascending part of the curve and fitting the descending part with a sum of three

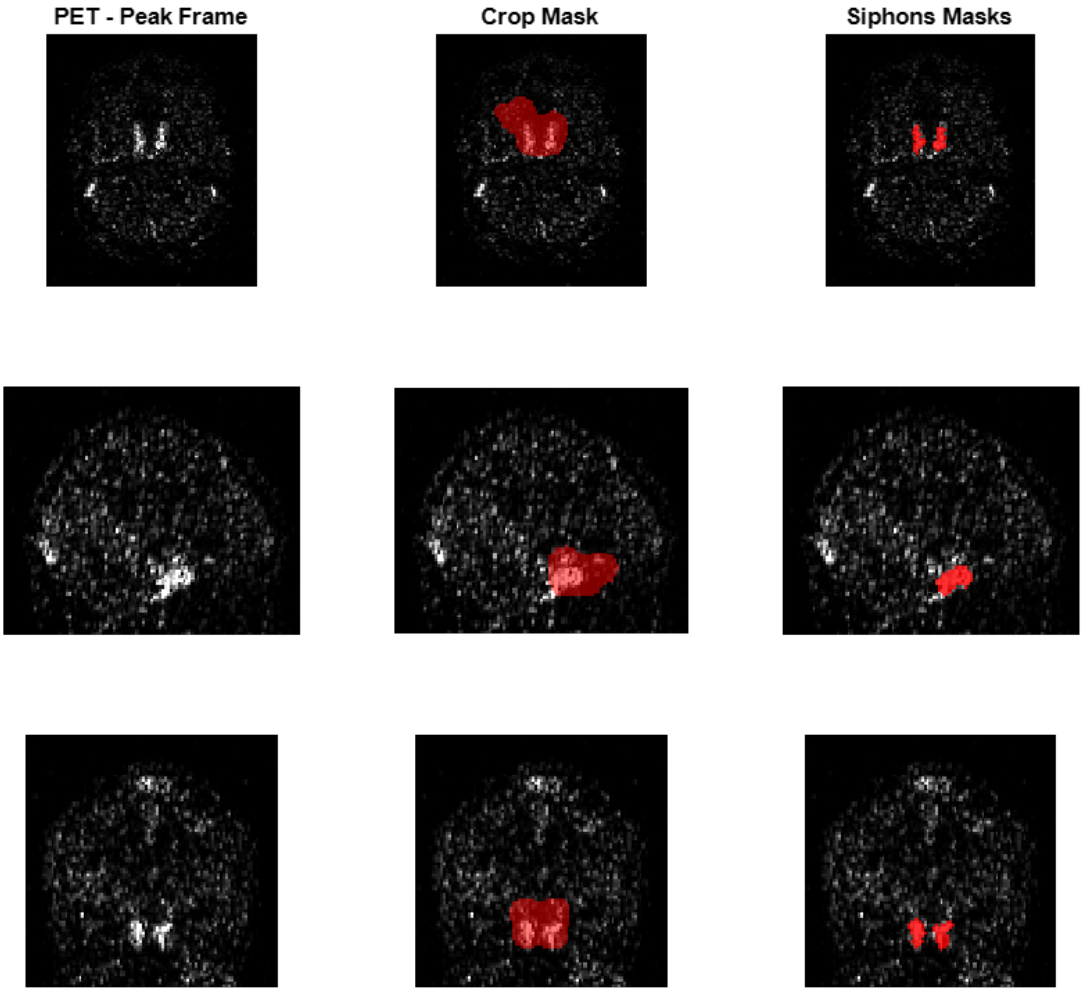

Figure 3.3: Representative result of siphons mask definition

Subject from Dataset 1. The left column displays various PET views (axial, sagittal, and coronal) at peak activity in the carotid siphons area. The center column shows an intermediate step before achieving optimal siphons segmentation, depicted on the right.

exponential functions (Parsey et al., 2000). Specifically, for each dataset, IDIFs were normalized and aligned based on the peak activity, allowing for the calculation of a representative mean curve. This mean curve was fitted using weighted non-linear least squares (WNLLS) (*lsqnonlin* MATLAB function) to estimate the model parameters. The model was then applied individually to each subject's IDIF, with parameter refinement to ensure fitting quality. Model weights for each PET mid-frame were defined as the reciprocal of the length of the respective scanning interval. Particular attention was placed on the last samples; their weights were reduced by a factor of ten if they tended to show aberrant increases due to noise. A representative result of this procedure is depicted in Fig. 3.4.

For Dataset 1, where the IDIF was extracted for the first time, the physiological significance of the final IDIF was evaluated by fitting a linear model with the injected dose of radiotracer

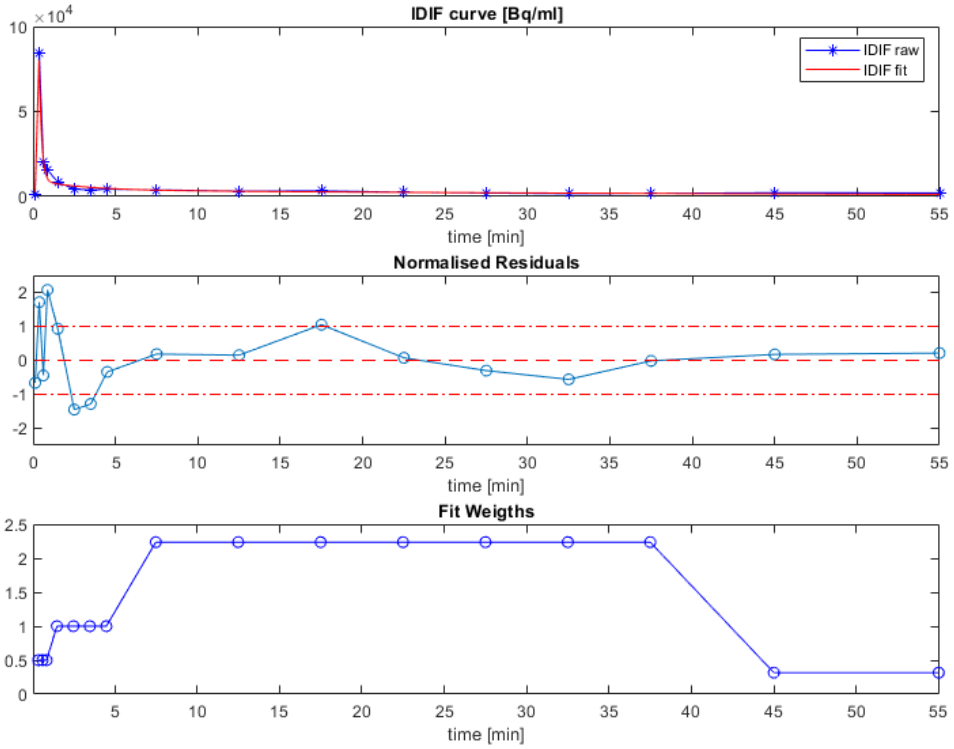

Figure 3.4: Representative outcome of IDIF fitting

Model fit, normalised residuals and model weight are illustrated for a subject in Dataset 1

normalized by body weight (DW) as the independent variable and the IDIF area under the curve (AUC) as the dependent variable. The resulting R^2 value of the linear relationship was 0.44, indicating a good reliability of the extracted IDIFs.

3.2.3 K_1 estimation

After extracting the TAC and IDIF, the parameter K_1, which represents the blood-to-brain influx rate constant, was estimated using the blood-free 1T1K-IDIF model (see Section 3.2). The first analysis included the computation of this parameter at region of interest (ROI)-level. The previously described assumptions allowed to derive a simple mono-compartmental dynamic in the first minutes after tracer injection, which is mathematically represented by the following system of equations:

$$\begin{cases} \dot{C}_1(t) = K_1 \text{IDIF}(t), \quad C_1(0) = 0 \\ C(t) = C_1(t) \end{cases} \tag{3.3}$$

The only measured quantity ($C(t)$) is the tracer's concentration in the tissue, represented by PET signal, while the input function is represented by the IDIF. Furthermore, K_1 estimate is achievable by using the gold-standard weighted non-linear least squares (WNLLS) estimator

(*lsqnonlin* MATLAB function). The model weights are defined as:

$$\mathrm{w_{ROI}}(\mathrm{t_i}) = \mathrm{dt_i}\mathrm{C_{ROI}}(\mathrm{t_i}), \tag{3.4}$$

where $\mathrm{t_i}$ is the time instant, $\mathrm{dt_i}$ is the length of the scanning interval, and $\mathrm{C_{ROI}}(\mathrm{t_i})$ is the ROI average time activity at time $\mathrm{t_i}$ (Cobelli et al., 1982).

Furthermore, another advantage of the one-tissue model is the possibility for model linearization (Carson, 1993). The differential equation describing the tracer dynamic can be integrated on both sides, resulting in the following expression:

$$\mathrm{C_1}(\mathrm{t}) = \int_0^{\mathrm{t_{fit}(end)}} \mathrm{IDIF}(\tau)\,\mathrm{d}\tau \tag{3.5}$$

This approach avoids the need for iterative non-linear methods to estimate $\mathrm{K_1}$, allowing for the use of a linear estimator. Model weights are defined as in Eq. 3.4. Denoting the integral of the IDIF by the vector $\mathbf{x}$, the ROI TAC by $\mathbf{y}$, the vector of model weights by $\mathbf{w}$, and the $\mathrm{K_1}$ estimate by $\hat{\beta}$, the explicit formula for regional $\mathrm{K_1}$ estimation using weighted linear least squares (WLLS) is:

$$\hat{\beta} = \left(\mathbf{x}^{\mathrm{T}}\mathrm{w}\mathbf{x}\right)^{-1}\mathbf{x}^{\mathrm{T}}\mathrm{w}\mathbf{y} \tag{3.6}$$

In this study, $\mathrm{K_1}$ rate constant was estimated using both WNLLS (considered the gold standard) and WLLS methods. The aim was validating, in this context, the linear estimation technique, which offers significant computational advantages and facilitates extending the methodology to the voxel-level. The study evaluated the inter-subject correlation and the difference between the estimates obtained with the two algorithms and assessed the precision of ROI estimates using the coefficient of variation (CV).

Remarkably, before linear estimation, the IDIFs, the vector containing the lengths of the scanning intervals for weights definition, and the ROI TACs were all interpolated onto a denser virtual time grid. Designing this grid was a crucial algorithmic detail, as it was carefully optimized to ensure that the original PET sampling grid was fully contained within it. This required the step size of the virtual grid to be a divisor of the time points in the original sampling grid. This detail was essential for optimizing parameter precision and ensuring the success of the methodology.

A pivotal validation step involved determining the appropriate time interval for fitting the reduced model. For Dataset 2, the window length had already been optimized (Maccioni et al., 2024). Specifically, they selected the interval following tracer administration when the plasma parent fraction (PPf) was greater than 90% to ensure adherence to the study's assumptions,

resulting in a 4-minute time window for [^{11}C]-PBR28. They were also able to evaluate the correlation between K_1 estimates obtained from the reduced model fitted at different time intervals and the gold-standard K_1 of the two-tissue model. For Dataset 1, where K_1 estimates using full compartmental modelling were unavailable due to the absence of blood data, model fit was evaluated in windows of varying lengths between 0 and 10 minutes with both linear and non-linear algorithms. The selection criteria balanced the need to restrict model fitting to a short time window to maintain model hypotheses and the necessity to include sufficient data points for accurate model fitting. Evaluation metrics included the mean of ROI K_1 estimates, their precision (CV) and the sum of squares of weighted residuals (WRSS). Consistency with previous TSPO PET studies, where K_1 computations were performed (Jučaite et al., 2012), and information on [^{11}C]-PK11195 PPf population curves (Souza et al., 2021) were crucial for guiding the window selection. The results from the validation of the fitting windows, which were determined to have an optimal duration of 5 minutes for Dataset 1, as well as the validation of the linear estimation method, will be presented in Chapter 4.

3.2.4 Methodology extension to voxel-level and parametric mapping

As previously mentioned, the use of WLLS for parameter estimation theoretically allows for a straightforward translation of the methodology from regional to voxel-level. The algorithmic details remain the same as for linear ROI-level quantification, including the selected time interval for model fitting (see Section 3.2.3). However, noise could impact voxel-level TACs, potentially hindering the application of kinetic modelling (Kotasidis et al., 2014). Therefore, a rigorous validation procedure for voxel-wise K_1 estimates is essential.

Similar to ROI-level estimation, voxel-wise quantification was performed in MATLAB after selecting voxels within each scan's individual brain mask. Subsequently, the relationship between ROI-level K_1 estimates and the distribution of voxel-wise K_1 estimates within each region was evaluated. Specifically, this evaluation included assessing the inter-subject correlation between ROI voxel medians and ROI-level estimates, as well as calculating the mean relative difference (MRD) between ROI-level estimates and the respective voxel-wise K_1 distributions. Results of the validation process are reported in Section 4.3.

The resulting brain K_1 parametric maps were converted from MATLAB (.mat) format to NIfTI format before the normalization procedure, using ANTs software (Advanced Normalization Tools, https://github.com/ANTsX/ANTs). The obtained maps were co-registered to the MNI152 template. For each image, the transformation consisted of a combination of rigid, affine, and SyN (Symmetric Normalization) transformations, computed with the *antsRegistration* function. The obtained transformations were applied to individual K_1 maps using *antsApplyTransforms*. Subsequently, each normalized map underwent smoothing with a Gaussian ker-

nel of 5 mm full-width at half-maximum (FWHM). This operation, performed with the FMRIB Software Library (FSL, version 6.0.3) function *fslmaths*, aimed to remove residual noise in the K_1 maps.

3.3 Statistical analysis

The statistical analysis that will be presented aimed to deepen the physiological significance of the extracted parameter, assessing its adherence to the study hypothesis and previous studies. The analysis was initially carried out at the regional level and subsequently extended to the voxel level. At both levels and across all datasets, the main investigations included assessing potential differences in the blood-to-brain influx rate between healthy subjects and patients with psychiatric disorders, further exploring the possible link between K_1 and subjects' demographics. Another important evaluation involved examining the potential connection between this microparameter and markers of peripheral inflammation. For this purpose, C-reactive protein (CRP) blood concentration was available for Dataset 1, while a direct marker of peripheral inflammation was not available for Dataset 2. Importantly, for Dataset 1, which included both healthy controls and patients diagnosed with MDD, all available participants were included in the investigations. For Dataset 2, which comprised healthy participants (HC and STRESS), individuals at Ultra-High Risk for Psychosis (UHRP), and patients diagnosed with Schizophrenia (SCZ), all available subjects were included in the investigations, except for the second scan of the 7 SCZ patients from the TSPO blocking study (Marques et al., 2021).

3.3.1 ROI-level analysis

This level of statistical analysis was fully performed using MATLAB R2022a (MathWorks). Lilliefors tests were conducted using *lillietest*, t-tests with *ttest2*, correlations with *corr*, and analysis of covariance (ANCOVA) with *anovan*. The latter function performs an analysis of variance (ANOVA) (Constrained Type III sum of squares) and accommodates continuous factors, allowing for the conduction of ANCOVA. The significance level for the reported analysis was set at $\alpha = 0.05$. A Lilliefors test for normality was conducted for the samples prior to every parametric test application. If the Gaussianity test indicated non-normality, a Wilcoxon rank-sum test (MATLAB function *ranksum*) was employed in place of the t-test, and Spearman's correlation was used instead of Pearson's correlation. Importantly, for this ROI-level statistical analysis, the validated K_1 estimates derived from the linear estimator (WLLS) were utilized.

For Dataset 1, which includes healthy controls (HC) and major depressive disorder (MDD) patients, the regions under investigation were those studied in (J. J. Schubert et al., 2021), specifically the anterior cingulate cortex (ACC), prefrontal cortex (PFC), and insular cortex (INS). The

three ROIs were originally selected based on previous findings, motivated by their role in mood regulation (Goldin et al., 2008; Talbot & Cooper, 2006), together with previous suggestions of the involvement of the ACC in the link between inflammation and depression (Hannestad et al., 2012; Harrison et al., 2009). The PFC region is the aggregate of the medial and dorsolateral frontal cortex regions, and the ACC region is the aggregate of the ventral cingulate subcallosal gyrus, anterior cingulate gyrus, and dorsal anterior cingulate regions from the original parcellation (see Section 3.2.1). The aggregation method was the arithmetic mean of the corresponding ROIs. Then, for each region, an analysis of covariance (ANCOVA) was performed with group (HC or MDD), C-reactive protein (CRP) concentration, and the interaction between the two as factors. Subsequently, other features (gender, body weight, age, radiotracer injected dose) were added to the statistical model to assess their effect on the parameter of interest. From this investigation, the factors that resulted significant were further analyzed. In particular, group differences between genders were evaluated with a two-tailed unpaired t-test. The same statistical test was then applied to assess group differences between controls and patients. Finally, the association between CRP levels and regional K_1 was evaluated with Pearson's correlation. CRP values were log-transformed beforehand to achieve normality and enable the use of parametric tests, in accordance with previous research practices (Turkheimer et al., 2021). Although the ANCOVA did not show a significant effect of body weight on K_1, this relationship was further examined using Pearson's correlation, considering that collinearity with CRP (see Section 4.4.1) might have masked the effect. For this dataset only, SUVR and AUC30-60 of the lateral ventricle signal was available from previous studies (Turkheimer et al., 2021), and Pearson's correlation with this metrics was also evaluated after their logarithmic transformation.

For Dataset 2, which focuses on psychosis, the selected regions of interest were those investigated in (Bloomfield et al., 2016): frontal grey matter (GM), temporal GM, and total GM. The regional K_1 values were obtained for each region, analogous to Dataset 1, by averaging the values of their corresponding subregions. Insights from the analysis of Dataset 1 highlighted significant effects of certain demographics on K_1. Therefore, a preliminary sensitivity analysis on all the subjects with ANCOVA was conducted with gender, age, body weight, injected dose, and TSPO genotype as variables of interest. Subsequently, to assess the potential effect of the disease on the K_1 parameter, unpaired t-tests were used to identify differences specifically between the HC group (excluding STRESS and UHRP individuals) and patients with schizophrenia. Furthermore, upon suspecting a possible confounding factor in this comparison, an ANCOVA was conducted for these two groups, covarying for gender and body weight. Additionally, for this dataset, group differences in K_1 between genders were evaluated. Finally, Pearson's correlation between body weight and K_1 was examined.

Importantly, for the above-reported analyses, correction for multiple comparisons was un-

necessary due to the targeted selection of regions in each disease context, which is supported by the reported literature.

3.3.2 Voxel-level analysis

Statistical analysis at the voxel level was performed using the FMRIB Software Library (FSL, version 6.0.3). The *randomise* function was utilized for all analyses of K_1 maps, employing the general linear model (GLM) framework. The GLM is a flexible approach that models the relationship between observed data and explanatory variables. It is defined as:

$$\mathbf{Y} = \mathbf{X}\beta + \epsilon \tag{3.7}$$

where:

- $\mathbf{Y}$ represents the voxel-wise measurements (e.g., K_1 maps).
- $\mathbf{X}$ is the design matrix that encodes the experimental design, with each column representing different conditions, groups, or covariates.
- β is the vector of parameters to be estimated, indicating the contribution of each explanatory variable.
- ϵ is the error term.

Contrasts are specified to test specific hypotheses about the parameters in β. They are defined as a vector that combines the parameter estimates to examine differences or effects of interest. In this context, an unpaired t-test is a specific case of general linear model, where the design matrix $\mathbf{X}$ specifies the groups or conditions being compared. The t-test evaluates whether the difference between group means is significantly different from zero using the contrast vector $\mathbf{c} = [1, -1]$. This contrast tests whether the mean of the first group is significantly greater than the mean of the second group. Alternatively, the contrast vector $\mathbf{c} = [-1, 1]$ can be used to test the reverse hypothesis, assessing whether the mean of the second group is significantly greater than the mean of the first group. After fitting the GLM, the *randomise* function computes t-statistics for each parameter β to assess whether its estimated effect on $\mathbf{Y}$ is statistically different from zero. In addition to t-statistics, *randomise* employs Threshold-Free Cluster Enhancement (TFCE) for cluster-based inference, which adjusts for multiple comparisons without requiring an arbitrary threshold for cluster formation (Smith & Nichols, 2009). Importantly, all regressors were demeaned before being input into the *randomise* function.

For Dataset 1, an unpaired two-sample t-test was used to evaluate the group difference between HC and MDD patients in both directions. Subsequently, a GLM was constructed to assess

both the negative and positive effects of covariates (gender, age, injected dose, body weight) on K_1 maps. An additional GLM was implemented to assess the isolated effect of body weight, which approached but did not reach statistical significance in the initial model, indicating potential masking due to collinearity. Finally, a GLM was developed to examine the effect of C-reactive protein (CRP), whether negative or positive, following its log-transformation. Remarkably, one healthy subject, who lacked CRP quantification, was not included in the aforementioned analyses.

For Dataset 2, a GLM was conducted on all included subjects (see Section 3.3) to investigate the potential effects of gender, age, injected dose, TSPO genotype, and body weight on K_1, examining both positive and negative effects of these covariates. The potential effect of the disease on K_1 was assessed by evaluating the group differences between HC (excluding STRESS and UHRP subjects) and SCZ patients using a two-sample t-test in both directions. The same test was repeated with additional nuisance variables, specifically gender and body weight.

3.3.3 Imaging transcriptomics analysis

The final investigation presented in this work aimed to exploit the approach of integrating neuroimaging and transcriptomics data, known as Imaging Transcriptomics (Martins et al., 2021). The analysis was conducted using the Imaging Transcriptomics toolbox (Giacomel et al., 2022), a new package providing a complete pipeline. This toolbox enables the identification of gene expression patterns that correlate with specific neuroimaging phenotypes and performs gene set enrichment analyses (GSEA) to offer biological insights into the findings. This framework, which operates with Python 3, was applied to statistical maps representing the association between measures of peripheral inflammation and the blood-to-brain influx rate of PET tracers, aiming to identify the physiological substrates of the key findings of this work.

Specifically, the images under investigation were the maps of the t-statistics (outputs of the FSL *randomise* function, see Section 3.3.2) related to the negative linear association between the K_1 parameter and $\log(\mathrm{CRP})$ for Dataset 1 and the maps of the t-statistics related to the negative linear association between the K_1 parameter and body weight for both datasets. The software utilizes gene expression data from the Allen Human Brain Atlas (AHBA, http://human.brain-map.org/) and maps genetic and neuroimaging data into the same space using the Desikan-Killiany (DK) parcellation. For neuroimaging data, the average signal across all voxels in each parcel is considered in the following steps. A mass-univariate Spearman correlation analysis was selected from the package options to quantify the association between each gene's expression and the neuroimaging phenotype. To calculate statistical significance, permutation testing, which accounts for the spatial autocorrelation inherent in the imaging data, was employed. This method generates one thousand null spatial maps through spin rotations of cortical

regions and resampling of subcortical regions. The output of this analysis is a ranked list of genes with their respective correlation coefficients, uncorrected p-values, and False Discovery Rate (FDR)-corrected p-values.

Additionally, Gene Set Enrichment Analysis (GSEA) (Subramanian et al., 2005) was implemented to determine which categories of genes were significantly related to the imaging phenotype. The first gene set investigated was the "Lake" gene set, which includes genes expressed in 30 brain cell types (Lake et al., 2018). Other gene sets used for GSEA included "GO Biological Processes", "GO Cellular Components" and "GO Molecular Functions". The outputs of this analysis are tabular files containing, for each term of the gene set, the enrichment score (ES), uncorrected p-values, and FDR-corrected p-values. Specifically, the enrichment score (ES) reflects the extent to which a gene set is overrepresented at the top (positive score) or bottom (negative score) of the ranked gene list from the correlation analysis. The p-values indicate the significance of the observed enrichment, with the FDR-corrected p-values accounting for multiple comparisons.

Chapter 4

Results

4.1 Fitting window optimization

The methodological framework described in Section 3.2 necessitates defining a restricted time interval after tracer injection where PET data are fitted using a reduced kinetic model (1T1K-IDIF). This validation step was required for Dataset 1, since the methodology was applied for the first time. Insights from the scientific literature, combined with visual inspection of model fit and assessment of model fitting performance metrics, were crucial for optimizing the fitting window. The precision of parameter estimates (CV) and the evaluation of the absolute model estimates at different fitting intervals are depicted in Fig. 4.1 for Dataset 1. For this dataset, the suitable time interval for model fitting was determined to be 0-5 minutes. This choice was guided by previous findings on the metabolism of the radiotracer [^{11}C]-PK11195 and insights from prior works where the K_1 parameter was estimated using this tracer. Specifically, earlier studies indicated that more than 90% of [^{11}C]-PK11195 tracer remained intact after 5 minutes post-injection (Souza et al., 2021), which aligns with the kinetic modelling assumptions (see Section 3.2). Furthermore, selecting this window ensured that the mean absolute value of the K_1 rate constant was consistent with physiological values extrapolated from previous investigations with this first-generation tracer (Jučaite et al., 2012). Additionally, this interval ensures accurate parameter estimates, as assessed by the coefficient of variation (CV). Importantly, extending the window further would not only undermine the initial assumptions about kinetic modelling, but also lead to unacceptable model residuals and an unacceptable Weighted Residual Sum of Squares (WRSS), due to the inherent challenge of a simple mono-compartmental dynamic in accurately representing the experimental data.

Remarkably, the optimal windows were the same for both estimators used (weighted linear least squares (WLLS) and weighted non-linear least squares (WNLLS)).

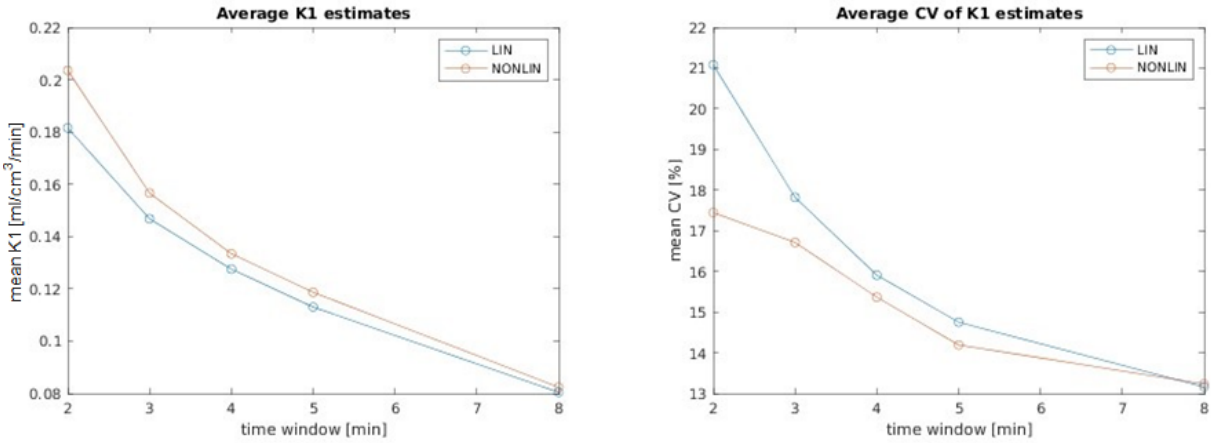

Figure 4.1: Fitting window definition (Dataset 1): mean K_1 estimates magnitude and precision (CV). Results related to WLLS are shown in blue, and results for WNLLS are shown in red.

4.2 Validation of linear least squares estimates

The linear estimates of K_1 were compared to those of the gold standard non-linear algorithm as reported in Section 3.2.4. For all datasets, the intra-subject correlations between the estimates obtained with the two methods were extremely high, as depicted in Fig. 4.2. Notably, only for Dataset 1, a limited number of linear ROI estimates, in a total of 5 subjects, were deemed unacceptable (close to zero) and discarded. This is likely due to the high level of noise in the related regional TACs and the limited signal-to-noise ratio of [^{11}C]-PK11195 data. For Dataset 2, all linear estimates were successfully obtained.

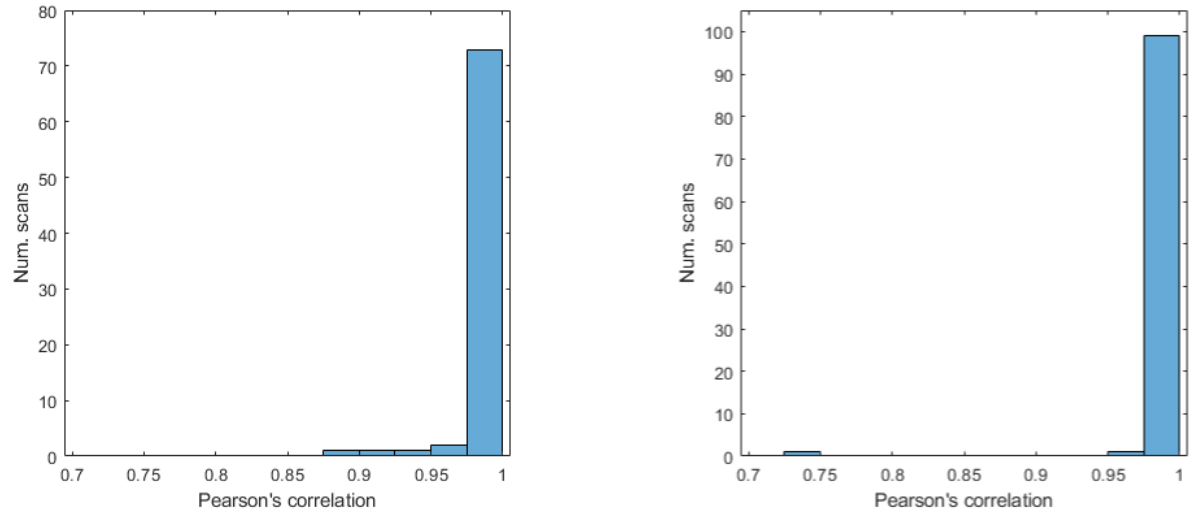

(a) Dataset 1 **(b)** Dataset 2

Figure 4.2: Distribution of intra-subject correlations between linear and non-linear algorithm ROI estimates.

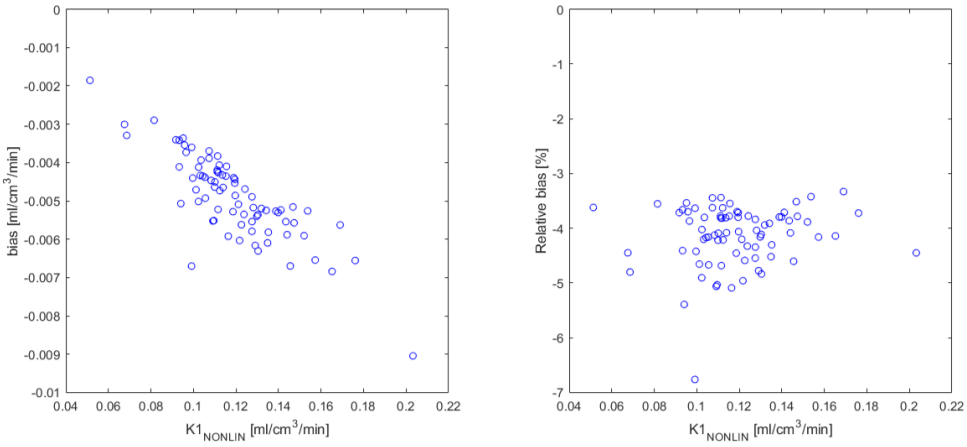

(a) Dataset 1

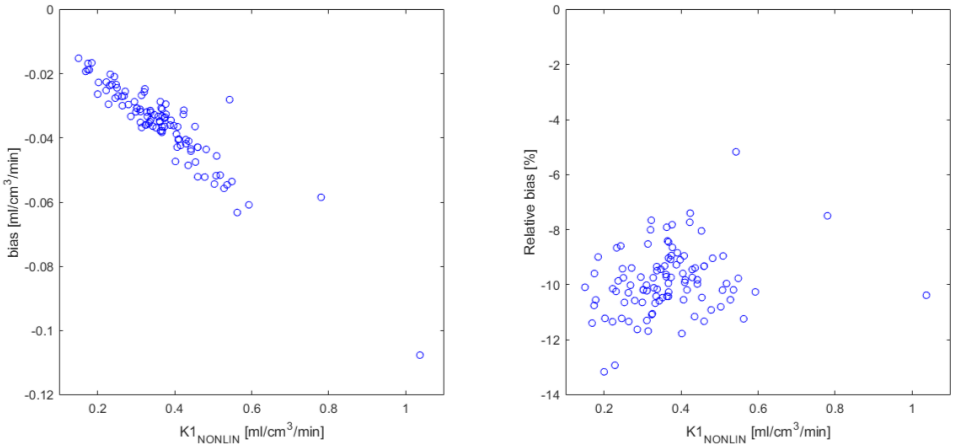

(b) Dataset 2

Figure 4.3: Bias and relative bias of linear with respect to non-linear algorithm estimates. Each dot represents the average across ROIs for one subject.

The bias and relative bias of the linear estimates with respect to the reference WNLLS parameter estimates showed a small underestimation by the linear algorithm, as depicted in Fig. 4.3. In particular, the magnitude of this underestimation was around 4% for Dataset 1 and 10% for Dataset 2.

The precision of the parameter estimates obtained with the two algorithms was comparable, as shown in Fig. 4.4. For Dataset 1, the average CV (%) was 14.2 $\pm$ 1.6 for WLLS and 14.2 $\pm$ 1.4 for WNLLS; for Dataset 2, it was 13.5 $\pm$ 2.6 for for the linear estimator and 12.8 $\pm$ 2.5 for the non-linear estimator.

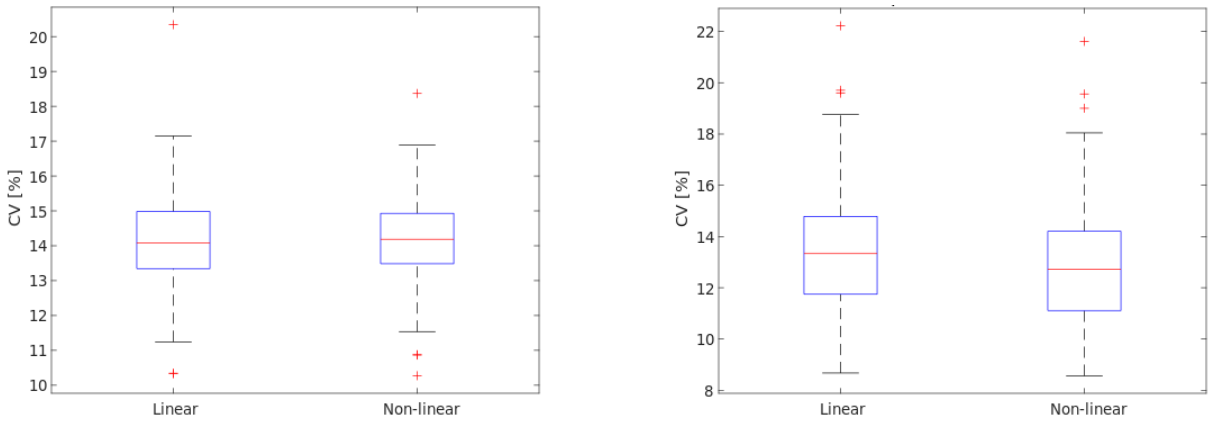

(a) Dataset 1 **(b)** Dataset 2

Figure 4.4: Distribution of subjects' average precision of the estimates (CV)

4.3 Validation of voxel-wise K_1 estimates

The level of agreement between voxel-wise estimates and ROI-level estimates was evaluated by examining the results in representative subjects and using quantitative measures. The first metric consists in the intra-subject correlation between ROI-level estimates and the median of voxel-wise estimates within corresponding regions. The results of this initial investigation are presented in Fig. 4.5. The intra-subject correlations were high, indicating strong agreement between the two types of estimates. Only isolated cases in Dataset 1 showed lower values, likely due to noisy dynamics and poor signal-to-noise ratio (SNR) of [^{11}C]-PK11195.

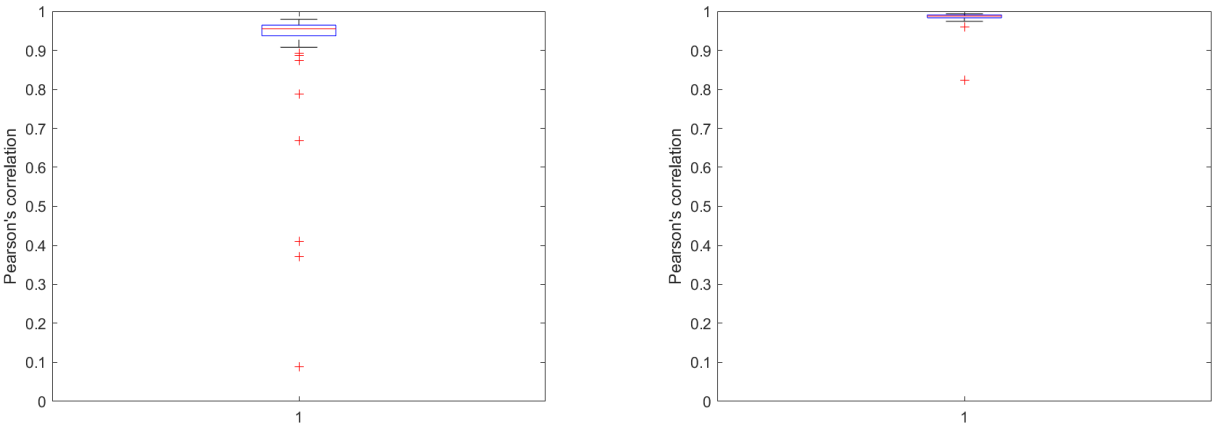

(a) Dataset 1 **(b)** Dataset 2

Figure 4.5: Distribution of intra-subject correlations between ROI estimates and voxels' medians within a region

A second metric used was the mean relative difference (MRD [%]), measured for each region, between the ROI-level estimate and the voxel-wise estimates within the ROI (Fig. 4.6). On average, voxel-level estimates tended to be moderately lower than their respective ROI-level estimates, with the magnitude of this difference varying across the three radiotracers. In Dataset 1, the underestimation was approximately 20% on average, whereas in Dataset 2, it is only 2%.

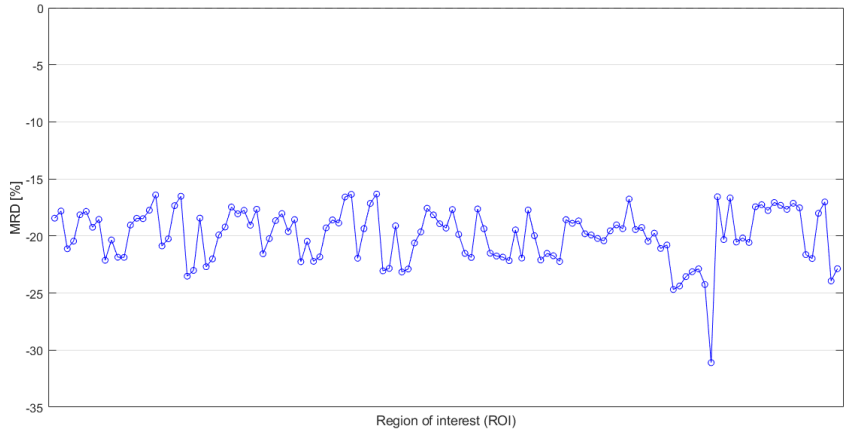

(a) Dataset 1

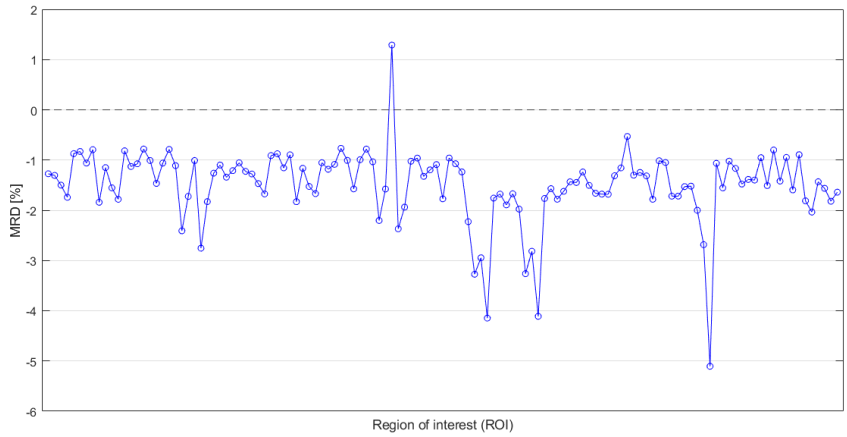

(b) Dataset 2

Figure 4.6: Mean relative difference (MRD %) between each ROI-level estimate and voxel estimates within the region. The x-axis represents the ROIs, and the MRD values were averaged across subjects. The minimum MRD was reached in the medulla oblongata for both datasets. The only case of positive MRD (%) was observed in the right lingual gyrus in Dataset 2.

Examples of the resulting K_1 parametric maps, after normalization to MNI space and Gaussian smoothing (FWHM = 5 mm), are shown for each dataset in Fig. 4.7

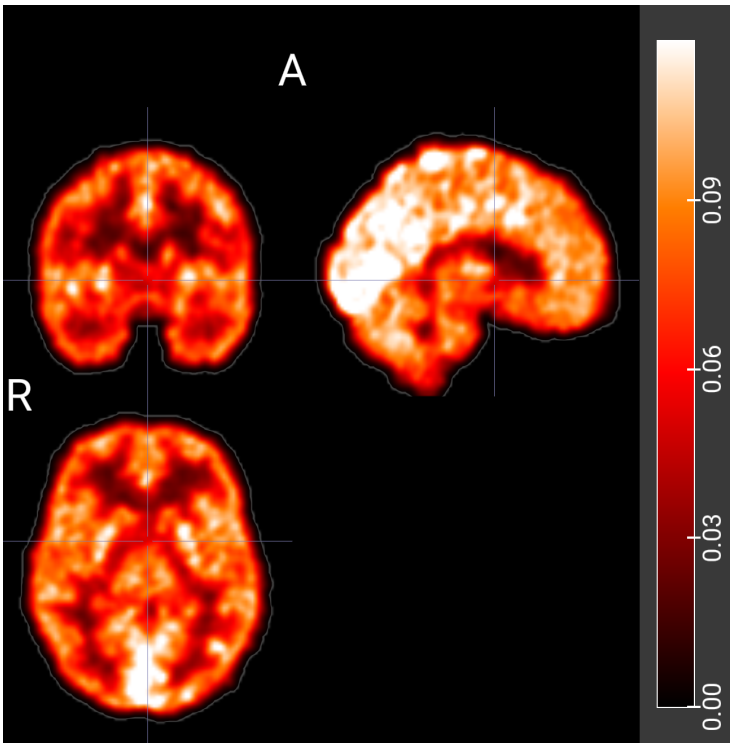

Dataset 1 ([^{11}C]-PK11195)

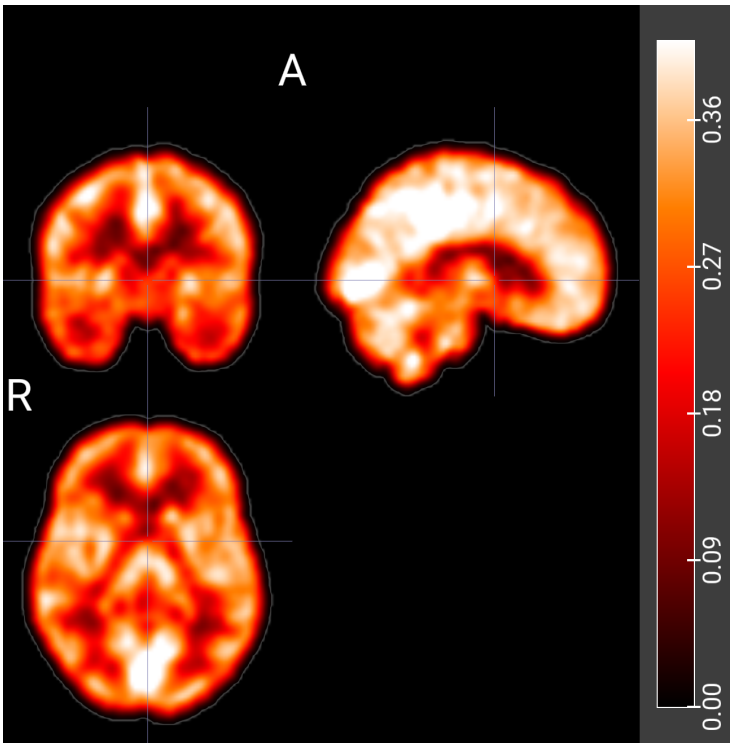

Dataset 2 ([^{11}C]-PBR28)

Figure 4.7: K_1 parametric maps [ml/cm^3/min]. All representative subjects were healthy controls. Maps are in MNI space, and a Gaussian filter (FWHM = 5 mm) was applied.

4.4 K_1 statistical analysis

4.4.1 ROI-level analysis

For Dataset 1, in the context of major depressive disorder, the first ANCOVA with group (HC vs. MDD), CRP, and their interaction as factors revealed significant effects of CRP and the interaction term in all the studied regions.

- **ACC**: No significant effect of group ($\mathrm{F} = 2.61, \mathrm{P} = 0.11$). CRP showed significant effects ($\mathrm{F} = 6.51, \mathrm{P} = 0.01$), as did the interaction between group and CRP ($\mathrm{F} = 4.90, \mathrm{P} = 0.03$).
- **PFC**: No significant effect of group ($\mathrm{F} = 2.53, \mathrm{P} = 0.12$). CRP showed significant effects ($\mathrm{F} = 5.93, \mathrm{P} = 0.02$), as did the interaction between group and CRP ($\mathrm{F} = 4.17, \mathrm{P} = 0.04$).
- **INS**: No significant effect of group ($\mathrm{F} = 2.20, \mathrm{P} = 0.14$). CRP showed significant effects ($\mathrm{F} = 6.40, \mathrm{P} = 0.01$), as did the interaction between group and CRP ($\mathrm{F} = 4.58, \mathrm{P} = 0.04$).

Moreover, by adding other covariates to the model (age, gender, body weight, injected dose), the interaction term between group and CRP lost its significance in all the ROIs, while gender revealed a significant effect in all three regions:

- **ACC**: The only significant effects were those of CRP ($\mathrm{F} = 5.81, \mathrm{P} = 0.02$) and gender ($\mathrm{F} = 6.41, \mathrm{P} = 0.01$).
- **PFC**: The only significant effects were those of CRP ($\mathrm{F} = 5.23, \mathrm{P} = 0.03$) and gender ($\mathrm{F} = 5.58, \mathrm{P} = 0.02$).
- **INS**: The only significant effects were those of CRP ($\mathrm{F} = 5.56, \mathrm{P} = 0.02$) and gender ($\mathrm{F} = 5.40, \mathrm{P} = 0.02$).

As anticipated by the ANCOVA, post-hoc tests revealed no significant difference between healthy controls' and depressed patients' blood-to-brain influx rate in any of the regions under investigation (two-tailed unpaired t-test, all p-values > 0.05) (Fig. 4.8). Conversely, there was a significant group difference between genders, as indicated by the two-tailed unpaired t-test (Fig. 4.9). Results of the statistical tests as well as an indication of the percentage gap between females' and males' average K_1 values are provided as follows:

- **ACC**: Male vs. female: $\mathrm{t} = -2.37, \mathrm{df} = 76, \mathrm{P} = 0.02, \mathrm{CI} = [-0.023, -0.002]$. On average, K_1 was 12.8 % higher in females compared to males.

- **PFC**: Male vs. female: $\mathrm{t} = -2.10, \mathrm{df} = 76, \mathrm{P} = 0.04, \mathrm{CI} = [-0.022, -0.001]$. On average, K_1 was 10.7 % higher in females compared to males.

- **INS**: Male vs. female: $\mathrm{t} = -2.25, \mathrm{df} = 76, \mathrm{P} = 0.03, \mathrm{CI} = [-0.024, -0.001]$. On average, K_1 was 11.7 % higher in females compared to males.

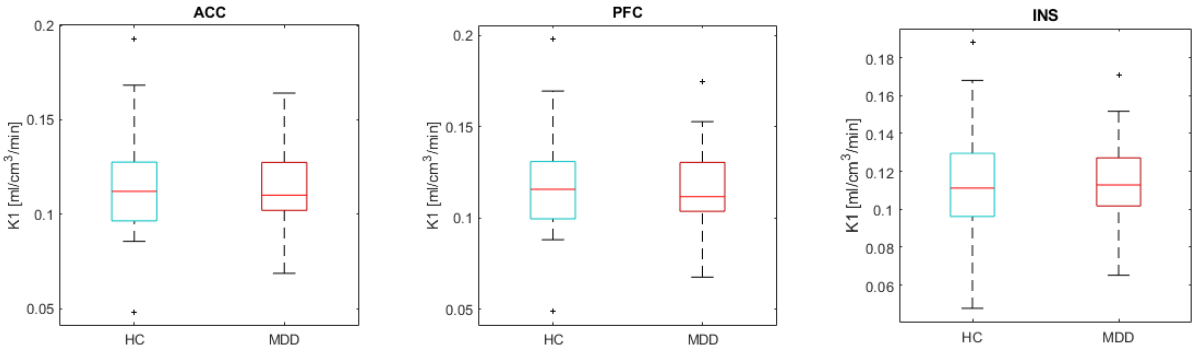

Figure 4.8: Distribution of K_1 in ACC, PFC, and INS, grouped by HC vs. MDD. No significant differences were found between the groups.

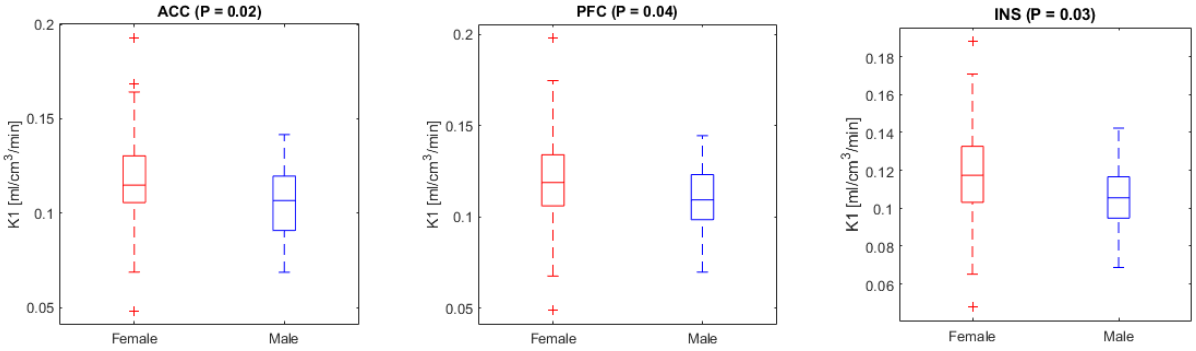

Figure 4.9: Distribution of K_1 in ACC, PFC, and INS, grouped by gender. P-values refer to the results of two-tailed unpaired t-tests.

Furthermore, investigation on the link between K_1 and C-reactive protein (CRP) blood concentration revealed significant negative linear association between the rate constant and the natural logarithm of CRP, as stated by Pearson's correlation (**ACC**: $\mathrm{r} = -0.30, \mathrm{P} = 0.008$; **PFC**: $\mathrm{r} = -0.31, \mathrm{P} = 0.006$; **INS**: $\mathrm{r} = -0.30, \mathrm{P} = 0.007$) (Fig. 4.10).

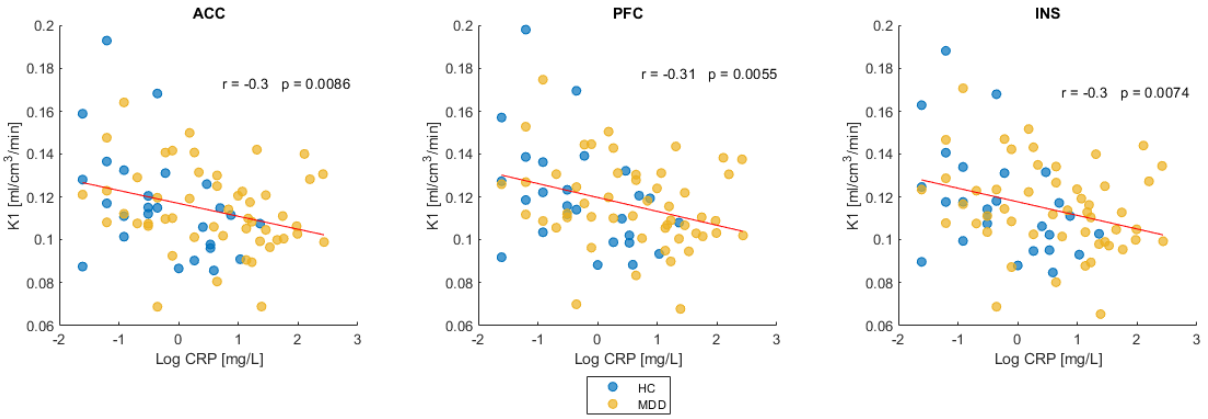

Figure 4.10: Scatter plots showing, for each region, the negative linear association between log(CRP) and K_1

Pearson's correlation suggested a negative trend but not a significant association between body weight and K_1 (**ACC**: $r = -0.18, P = 0.116$; **PFC**: $r = -0.17, P = 0.127$; **INS**: $r = -0.19, P = 0.099$). Remarkably, body weight was significantly positively correlated with log(CRP) (Pearson's $r = 0.33, P = 0.003$). Finally, the only significant association between the lateral ventricle TSPO signal and blood-to-brain influx rate was found in the prefrontal cortex, using the log-transformed version of the area under the curve (AUC) of the lateral ventricle signal (Pearson's $r = 0.28, P = 0.04$) (Fig. 4.11).

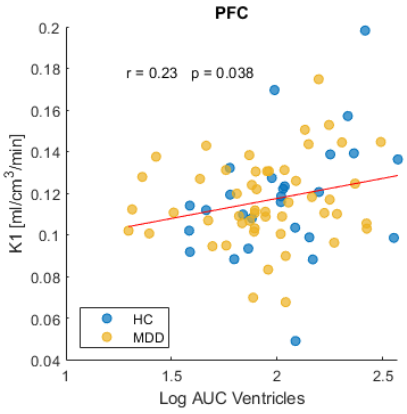

Figure 4.11: Scatter plots showing the positive linear association between the area under the curve (AUC) of the lateral ventricle TSPO signal and K_1, for PFC.

For Dataset 2, in the context of psychosis, the preliminary sensitivity analysis using ANCOVA (gender, age, injected dose, body weight, TSPO genotype) revealed significant effects of gender and body weight in all three areas. The effect of the injected dose was significant

only in the temporal grey matter, being just above the threshold for significance. However, the magnitude of this effect was considerably smaller compared to those of gender and weight and was not considered in the subsequent analyses.

- **Total GM**: significant effect of gender ($\mathrm{F} = 8.86, \mathrm{P} = 0.004$) and weight ($\mathrm{F} = 10.53, \mathrm{P} = 0.002$).
- **Temporal GM**: significant effect of gender ($\mathrm{F} = 8.12, \mathrm{P} = 0.005$), weight ($\mathrm{F} = 10.21, \mathrm{P} = 0.002$) The effect of dose was just below the threshold for significance ($\mathrm{F} = 4.17, \mathrm{P} = 0.044$).
- **Frontal GM**: significant effect of gender ($\mathrm{F} = 8.58, \mathrm{P} = 0.004$), weight ($\mathrm{F} = 10.74, \mathrm{P} = 0.002$).

A one-tailed t-test revealed a significant reduction of temporal GM K_1 in SCZ compared to HC (HC vs. SCZ: $\mathrm{t} = 1.99, \mathrm{df} = 65, \mathrm{P} = 0.02$) (Fig. 4.12) . No differences between HC and SCZ were found in total and frontal GM (all P-values > 0.05).

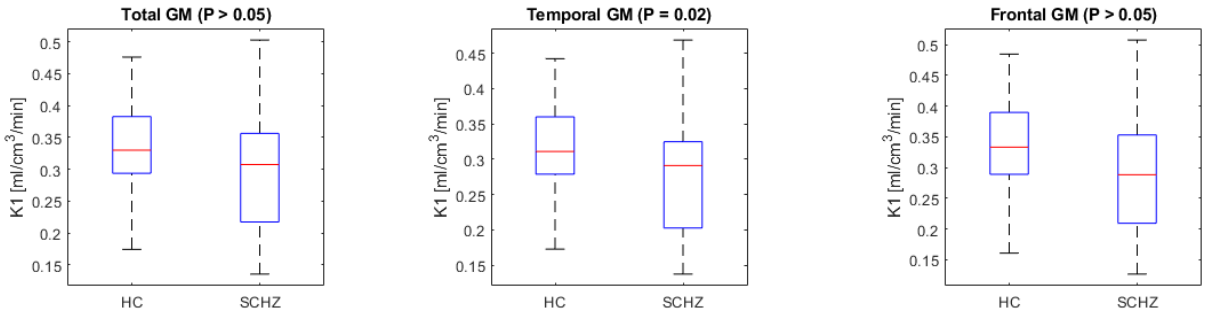

Figure 4.12: Distribution of K_1 in total GM, temporal GM, and frontal GM, grouped by HC vs. SCZ. P-values refers to the results of the one-tailed t-tests (HC>SCZ).

Furthermore, a deeper analysis of the sensitivity results revealed a significant group difference between genders, as indicated by two-tailed Wilcoxon rank-sum tests (after failure of the normality test) in all brain areas under investigation (Fig. 4.13). Notably, to provide an indication of the percentage gap between females and males, the medians of the groups were used instead of the means, given the non-Gaussian distribution of the data.

- **Total GM**: Male vs. female: $\mathrm{z} = -4.33, \mathrm{P} < 0.001$. On average, K_1 was 30.5 % higher in females compared to males.
- **Temporal GM**: Male vs. female: $\mathrm{z} = -4.30, \mathrm{P} < 0.001$. On average, K_1 was 26.5 % higher in females compared to males.

- **Frontal GM**: Male vs. female: $z = -4.27, P < 0.001$. On average, K_1 was 33.3 % higher in females compared to males.

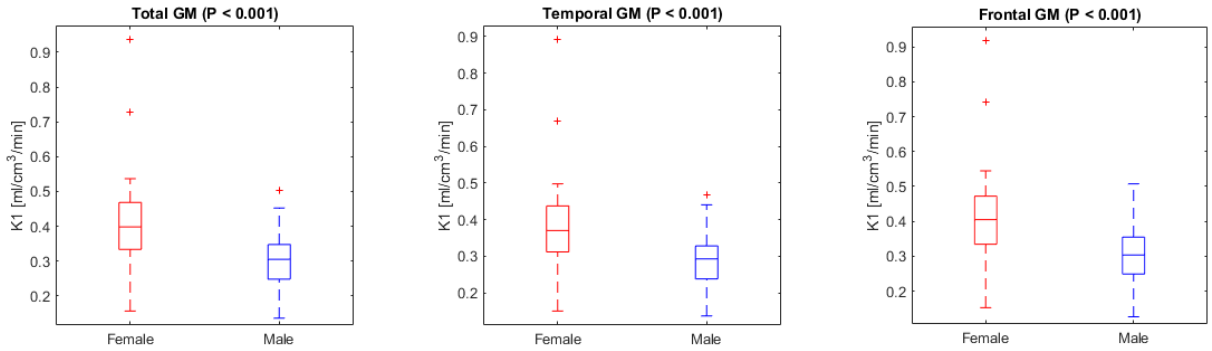

Figure 4.13: Distribution of K_1 in total GM, temporal GM, and frontal GM, grouped by gender. P-values refer to the results of the Wilcoxon rank sum tests.

Furthermore, there was a negative linear association between body weight and regional K_1 values, as indicated by Pearson's correlations (**Total GM**: $r = -0.42, P < 0.001$; **Temporal GM**: $r = -0.41, P < 0.001$; **Frontal GM**: $r = -0.43, P < 0.001$) (Fig. 4.14).

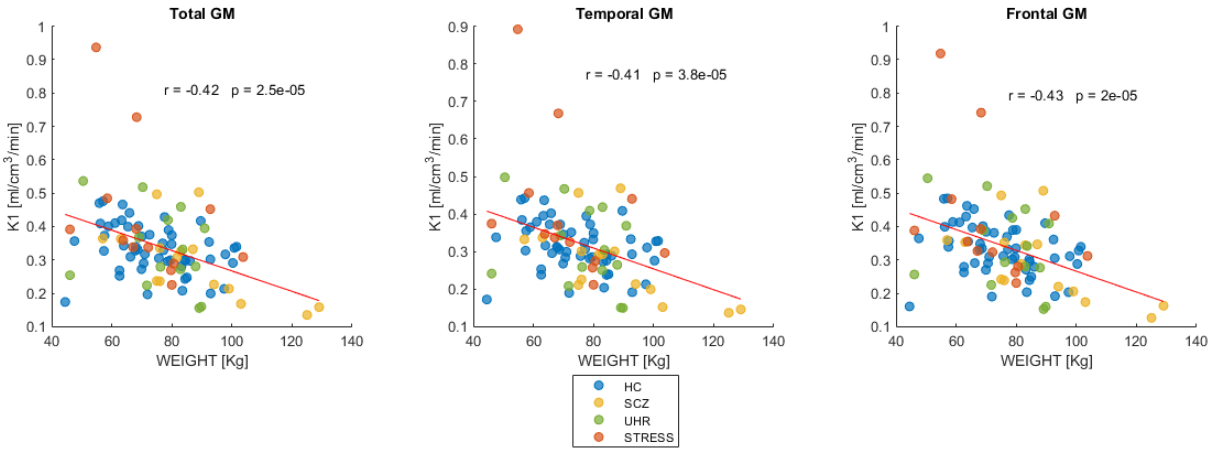

Figure 4.14: Negative linear association between body weight and K_1 in total GM, temporal GM, and frontal GM

Finally, the higher body weight of SCZ patients compared to HC (one-tailed t-test, $P = 0.003$), along with the disproportionate number of males and females in the SCZ cohort relative to HC, with a large prevalence of males in the pathological group (see Table 3.2), underscored

the necessity of adjusting for these potential confounding factors in examining group differences between HC and SCZ. After including body weight and gender as covariates in an ANCOVA, alongside the group factor (HC vs. SCZ), the group factor did not demonstrate significance in any region (all P-values > 0.05). However, weight continued to exhibit significant effects, while gender showed significance only in total GM, with levels just above the threshold of significance in temporal and frontal GM.

- **Total GM**: no significant effect of group ($\mathrm{F} = 0.29, \mathrm{P} = 0.59$); significant effect of weight ($\mathrm{F} = 5.87, \mathrm{P} = 0.02$) and gender ($\mathrm{F} = 4.27, \mathrm{P} = 0.04$).

- **Temporal GM**: no significant effect of group ($\mathrm{F} = 1.03, \mathrm{P} = 0.31$); significant effect of weight ($\mathrm{F} = 4.88, \mathrm{P} = 0.03$); the effect of gender was just above threshold for significance ($\mathrm{F} = 3.82, \mathrm{P} = 0.055$).

- **Frontal GM**: no significant effect of group ($\mathrm{F} = 0.22, \mathrm{P} = 0.64$); significant effect of weigth ($\mathrm{F} = 6.21, \mathrm{P} = 0.02$); the effect of gender was just above threshold for significance ($\mathrm{F} = 3.88, \mathrm{P} = 0.053$).

Importantly, what emerges from this latter investigation is that in the temporal GM, where a significant decrease in K_1 was found in SCZ, the disease's effect ceases to be significant after adjusting for the confounding effect of body weight. This correction helped mitigate any misleading results in the group comparison.

4.4.2 Voxel-level analysis

The relevant results of the statistical analysis on parametric maps are subsequently reported. For each finding, a map of the "raw" t-statistics will be depicted to allow for comparison between spatial patterns observed in the different datasets. Moreover, a map of the t-statistics with the significant clusters is depicted. When referring to statistical significance in this context, it indicates that the p-value adjusted for multiple comparisons with TFCE (see Section 3.3.2) is not greater than 0.05.

For Dataset 1, the unpaired two-sample t-test did not reveal any significant differences between HC and MDD patients in either direction. The GLM demonstrated a significant effect of gender, specifically a widespread increase in K_1 in females compared to males (Fig. 4.15a, 4.15b). The model did not identify any other significant effects among the covariates studied. However, as previously noted, body weight exhibited a negative trend that reached statistical significance when assessed independently in a separate model. (Fig. 4.16a, 4.16b). The final

GLM, designed to investigate the effect of $\log(\mathrm{CRP})$ on brain-to-blood tracer influx rate, revealed brain areas of significant negative association between the log-transformed CRP levels and K_1 (Fig. 4.17a, 4.17b).

For Dataset 2, the preliminary GLM with covariates revealed a significant effect of gender, with a widespread increase in K_1 in females compared to males (Fig. 4.15c, 4.15d). Additionally, the model identified areas with significant negative effects of body weight (Fig. 4.16c, 4.16d). The two-sample unpaired t-test did not reveal any significant differences between HC and SCZ patients, even after adjusting for the confounding effects of gender and body weight.

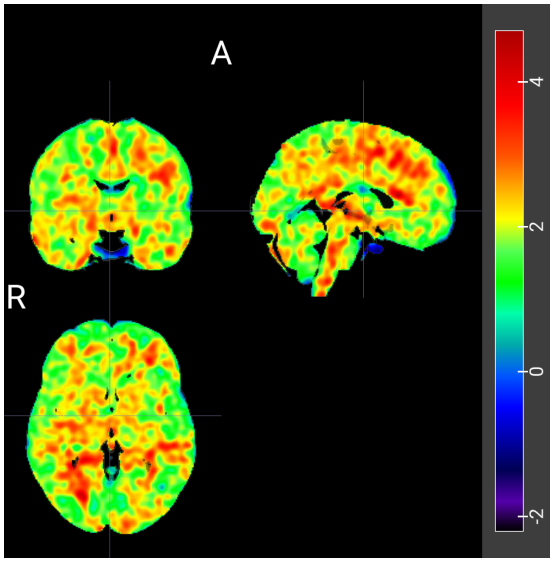

(a) Dataset 1: t-statistics.

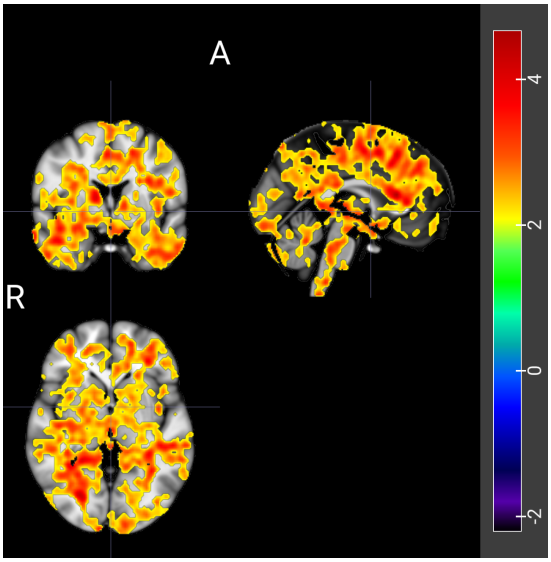

(b) Dataset 1: thresholded t-statistics.

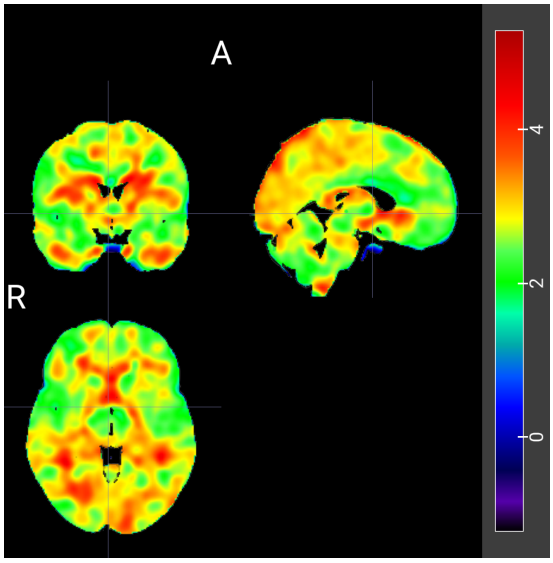

(c) Dataset 2: t-statistics.

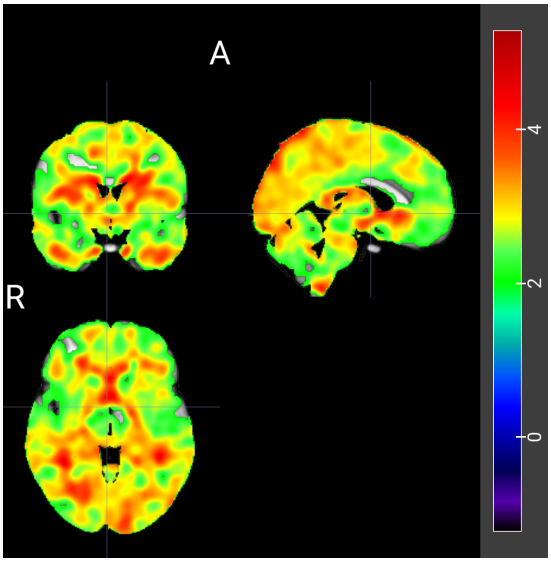

(d) Dataset 2: thresholded t-statistics.

Figure 4.15: Comparison of t-statistics maps for **gender effect (F > M)** across the two datasets. Each row displays the t-statistics map (left) and the thresholded t-statistics map (right) with corrected $P < 0.05$.

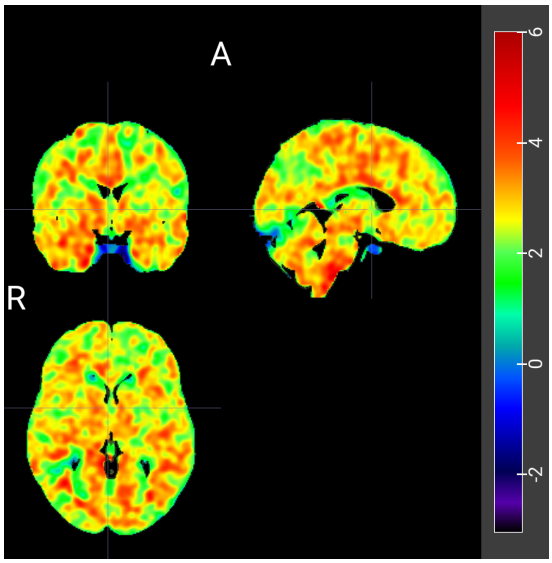

(a) Dataset 1: t-statistics.

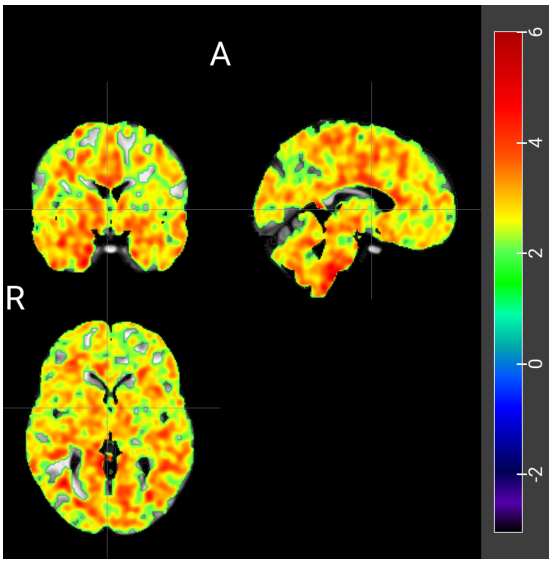

(b) Dataset 1: thresholded t-statistics.

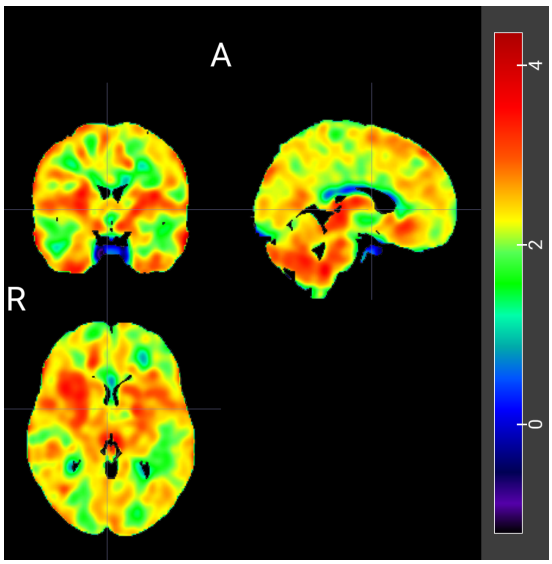

(c) Dataset 2: t-statistics.

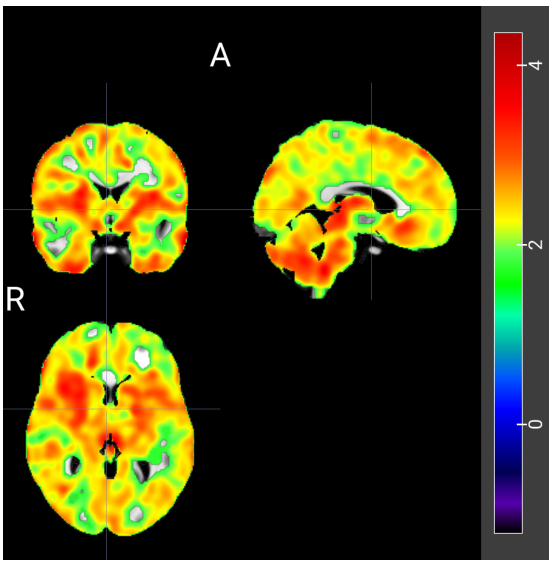

(d) Dataset 2: thresholded t-statistics.

Figure 4.16: Comparison of t-statistics maps for **negative effect of body weight** across datasets 1 and 2. Each row displays the t-statistics map (left) and the thresholded t-statistics map (right) with corrected $P < 0.05$.

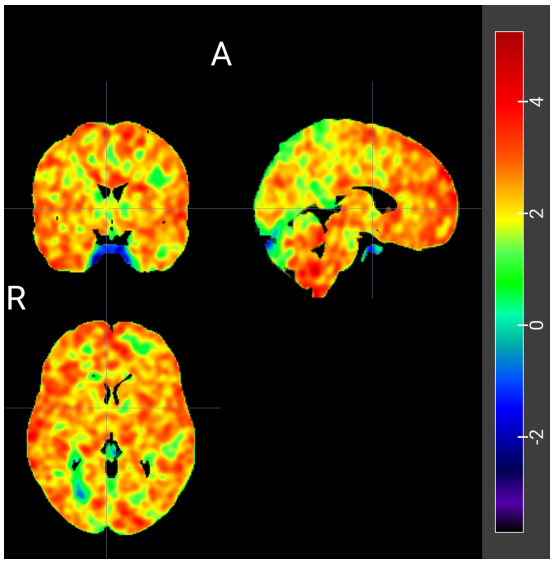

(a) Dataset 1: t-statistics.

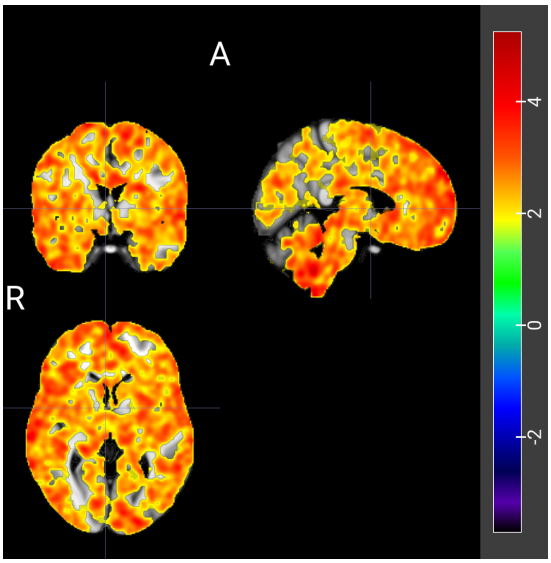

(b) Dataset 1: thresholded t-statistics.

Figure 4.17: T-statistics maps for the **negative effect of log(CRP)** on the K_1 parameter. The left panel shows the t-statistics map, while the right panel displays the thresholded t-statistics map with corrected $P < 0.05$.

When comparing the spatial extent of the observed effects across all datasets, several considerations emerge. Firstly, the effect of gender (F > M) was consistent across all datasets, showing no distinct pattern and being widespread throughout the brain, with symmetry between hemispheres (Fig. 4.15a,4.15c). Regarding the negative effect of body weight, it was broadly distributed in Dataset 1, with only a marginally notable cluster of higher magnitude observed in the brainstem (Fig. 4.16a). In Dataset 2, the effect was again substantially widespread and symmetric across hemispheres, with a more elevated impact extending to areas where it was less pronounced in dataset 1, including parts of the cerebral white matter, subcortical areas, and the cerebellum (Fig. 4.16c).

In Dataset 1, the negative effect of CRP on K_1 was significant across various cortical regions. This effect was particularly pronounced and widespread in the frontal areas, as well as in a large region encompassing the cerebellum and brainstem, spanning the fourth ventricle (Fig. 4.17a). Moreover, an intriguing, albeit partial, correspondence can be observed between these patterns and those representing the negative effect of body weight in the same dataset (Fig. 4.16a), particularly in terms of the elevation observed in the brainstem and frontal lobe.

4.4.3 Imaging transcriptomics

For this analysis, the images examined were maps of the t-statistics related to the negative linear association between the K_1 parameter and $\log(CRP)$ (Dataset 1) and the inverse linear association between K_1 and body weight (datasets 1 and 2).

Regarding the effect of C-reactive protein in Dataset 1, Gene Set Enrichment Analysis (GSEA) revealed no significant associations with brain cell types (Lake gene set), cellular components, or molecular functions after FDR correction. However, among the biological processes, genes associated with "Peptide Antigen Assembly With MHC Protein Complex (GO:0002501)" were found to be significantly overrepresented after FDR correction for multiple comparisons (ES = 0.673, FDR-corrected $P < 0.05$).

Concerning the effect of body weight in Dataset 1, GSEA revealed no significant associations with brain cell types (Lake gene set) or cellular components. Conversely, genes associated with three biological processes were found to be significantly underrepresented after correcting for multiple comparisons: "Receptor Metabolic Process (GO:0043112)" (ES = -0.624, FDR-corrected $P < 0.05$); "DNA Modification (GO:0006304)" (ES = -0.651, FDR-corrected $P < 0.05$); "Regulation Of Mitochondrial Fission (GO:0090140)" (ES = -0.710, FDR-corrected $P < 0.05$). Additionally, among the molecular functions, genes related to "Voltage-Gated Monoatomic Ion Channel Activity (GO:0005244)" were significantly underrepresented (ES = -0.666, FDR-corrected $P < 0.05$).

Finally, in regard to the negative effect of body weight in Dataset 2, GSEA revealed no significant associations with brain cell types, cellular components, or molecular functions after FDR correction. Nevertheless, gene sets related to three different biological processes were found to be significantly overrepresented: "tRNA Aminoacylation For Protein Translation (GO:0006418)" (ES = 0.578, FDR-corrected $P < 0.05$); "Regulation Of Ubiquitin Protein Ligase Activity (GO:1904666)" (ES = 0.683, FDR-corrected $P < 0.05$); "Cytoplasmic Translation (GO:0002181)" (ES = 0.702, FDR-corrected $P < 0.05$). On the other hand, gene sets related to two different biological processes were found to be significantly underrepresented: "Eye Morphogenesis (GO:0048592)" (ES = -0.587, FDR-corrected $P < 0.05$); "Detection Of Chemical Stimulus Involved In Sensory Perception Of Bitter Taste (GO:0001580)" (ES = -0.602, FDR-corrected $P < 0.05$).

Chapter 5

Discussion

5.1 Methodological advancements

This work presents a significant methodological advancement in mapping the blood-to-brain exchange of TSPO PET radiotracers. The new blood-free methodology (Maccioni et al., 2024) was successfully validated for the first-generation tracer [^{11}C]-PK11195. Especially for this radiotracer, the methodology assumes a crucial importance, being the plasma-based quantification unfeasible, due to the low free fraction in plasma (Turkheimer et al., 2007). For both TSPO radiotracers under investigation, including [^{11}C]-PBR28, the methodology was further extended to the voxel level. This extension was enabled by the use of a linear estimation method, whose estimates showed excellent agreement with those of the non-linear estimator (see Section 4.2). In the original work where the novel methodology was developed (Maccioni et al., 2024), high and variable bias was reported for the 1T1K-IDIF K_1 estimates. This bias depended on the variability of the IDIF in approximating blood input functions, typically leading to overestimation compared to the gold standard K_1 estimates obtained using the 2T2K-C_p compartmental model with blood data. Consequently, while this parameter can be used to quantify inter-subject differences in tracer delivery, the high bias renders it unsuitable for absolute quantification. The linear estimation methodology employed in the present study offers a significant advantage in terms of computational efficiency compared to iterative estimation procedures. Additionally, its slight tendency to underestimate K_1, relative to estimates obtained with the nonlinear algorithm (see Section 4.2), may help mitigate the overestimation observed by Maccioni et al. (2024) in the reduced model with IDIF.

Moreover, the transition from the ROI to the voxel level was supported by the optimal alignment between estimates at the two levels (see Section 4.3). This was evidenced by very high intra-subject correlations between regional estimates and the voxel medians within ROIs. Moreover, the mean relative difference of the voxel estimates with respect to their corresponding

ROI-level estimates was limited, with only a small tendency for average underestimation at the voxel level. This underestimation could be attributed to the noisy dynamics of TSPO PET voxel TACs, which may have impacted the estimation procedure, resulting in some voxel estimates being close to zero. This is supported by the observation that the mean relative difference was higher for [^{11}C]-PK11195, which is known to exhibit a lower signal-to-noise ratio compared to second-generation tracers.

The methodology enabled the computation of K_1 parametric maps with high definition and physiological relevance. As proof of this significance, the maps highlight and clearly distinguish areas of higher perfusion, such as the grey matter, compared to those of lower perfusion, such as white matter.

5.2 Physiological insights from key findings

Of great importance, the novel non-invasive methodology not only replicated previous findings but also suggested new insights that could prove fundamental for further technological advancements in neuroinflammation quantification, in a transdiagnostic context. Before discussing the main findings of this study, it is worth to reiterate the physiological meaning of the blood-to-brain influx rate constant K_1. This parameter represents the rate at which the tracer crosses the blood-brain barrier (BBB) from plasma and consists in the product of cerebral blood flow (blood perfusion) and the tracer's BBB extraction fraction (Renkin, 1959).

5.2.1 Peripheral inflammation and TSPO tracers influx rate

The primary finding of this study is the negative association between markers of peripheral inflammation and measures of blood-to-brain exchange of TSPO PET radiotracers. This result was consistently observed at both the regional and voxel levels in the dataset where C-reactive protein (CRP) measurements were available. Specifically, for Dataset 1 (BIODEP study), a reduction in blood-to-tissue TSPO ligand perfusion was indicated, in a previous work, by an inverse relationship between blood-to-CSF exchange parameters and CRP levels, with elevated CRP levels corresponding to lower SUVR and AUC30-60 of the TSPO signal in the lateral ventricle for both MDD patients and healthy controls (Turkheimer et al., 2021).

The new finding gains further credibility when considering the significant positive association between the K_1 parameter in the prefrontal cortex and the lateral ventricle AUC30-60, as measured in the previous study investigating Dataset 1. This suggests strong coherence between the two measures of blood-to-tissue tracer exchange and supports the physiological relevance of the K_1 parameter obtained with the novel blood-free methodology. Given that no effect of the psychiatric disease on the K_1 parameter was observed, these results support the idea of a

disease-agnostic link between increased peripheral inflammation and reduced delivery of TSPO radiotracers to the brain. Supporting this hypothesis, elevated serum peripheral C-reactive protein (CRP), induced by IFN-α injection in healthy individuals (FLAME study), was associated with reduced brain barrier permeability, as indicated by lower K_1 rate constants for the TSPO tracer [^{11}C]-PBR28 (Nettis et al., 2020; Turkheimer et al., 2021). Remarkably, the latter finding was replicated with the novel non-invasive methodology for K_1 estimation (Maccioni et al., 2024).

The present study cannot determine whether the observed inverse association between CRP and K_1 reflects an effect of cerebral blood flow or extraction. However, current literature suggests that reduced extraction is the primary mechanism for decreased tracer exchange (Turkheimer et al., 2021). PET radioligands, which are typically lipophilic, are tought to cross the blood-brain barrier via a transcellular route (Bagchi et al., 2019). The exact mechanisms for their passage through other layers of the barrier, such as gaps between astrocytic end-feet or aquaporin channels, are less understood and require further research. Interestingly, given that TSPO ligands have a molecular weight and lipophilicity similar to other lipid-soluble drugs, it is possible that reduced transport of these small lipophilic molecules could contribute to drug resistance (Turkheimer et al., 2021). Additionally, research involving the FLAME study cohort identified changes in the availability of free ligand in the plasma after peripheral immune challenges. Specifically, higher peripheral inflammation was associated with increased ligand binding to plasma proteins and decreased ligand availability for brain entry (Nettis et al., 2020). Given the collinearity between plasma protein binding and C-reactive protein (CRP) blood levels, other investigations on the same cohort studied their interaction with the parameter K_1. Partial regression between K_1 and CRP, controlling for plasma protein binding (f_p), still showed a significant association for GM tissue (Turkheimer et al., 2021). Additionally, when they directly corrected the transfer rate K_1 by multiplying it with f_p, they found the same significant associations between tracer perfusion and CRP for both CSF and GM. Therefore, although this is insufficient to disentangle the effects of CRP and f_p on K_1, it suggests that the observed reduction in perfusion could be due to the direct influence of peripheral inflammation on the permeability of the barrier to TSPO radiotracers. However, the present work did not investigate the effect of tracer binding to plasma proteins.

Moreover, although recent research found no significant changes in [^{11}C]-PBR28 radiotracer kinetics associated with alterations in cerebral blood flow, this evidence is insufficient to rule out the influence of cerebral blood perfusion on TSPO tracer delivery and uptake.

Insights from imaging transcriptomics analysis can provide valuable information about the underlying mechanisms. This analysis revealed a significant overrepresentation of genes involved in peptide-antigen assembly with Major Histocompatibility Complex (MHC) protein

complexes. According to the official definition (https://amigo.geneontology.org), this biological process involves the binding of a peptide to the antigen-binding groove of an MHC protein complex, which is crucial for antigen presentation to immune cells. For example, MHC class I molecules are expressed on the luminal side of brain endothelial cells, which are capable of antigen presentation (Galea et al., 2007). Additionally, both microglia and astrocytes can function as antigen-presenting cells (APCs) (Gimsa et al., 2013). Specifically, microglia express MHC class II readily upon activation both in vivo and in vitro, whereas astrocytes express MHC class II during prolonged inflammation in vivo (Kreutzberg, 1996) or in vitro upon stimulation by interferon-γ (Aloisi et al., 1999).

These cells may interact at the blood-brain barrier (BBB), potentially modulating its permeability. A recent study (Haruwaka et al., 2019) used a peripheral chronic LPS model to demonstrate that microglia respond to inflammation by becoming activated and migrating toward brain blood vessels before any detectable change in BBB permeability occurs. Although this model involves severe peripheral immune activation that eventually disrupts the BBB, the initial interactions between microglia and endothelial cells help maintain BBB integrity through the expression of the tight-junction protein Claudin-5. Similar protective effects of microglia on BBB stability during inflammation have also been reported in vitro (Spampinato et al., 2022). Furthermore, recent work (Suo et al., 2023) suggests that activated astrocytes also play a role in protecting BBB integrity.

Furthermore, future investigation could explore the role of the BBB's basement membrane, which is a highly organized extracellular matrix consisting of two distinct layers: the endothelial-derived layer and the astrocyte (glial)-derived layer (Galea, 2021). Located in the space between these layers are CD163-positive perivascular macrophages (Mato et al., 1996). These macrophages express surface molecules that allow them to respond to systemic inflammation, as well as antigen presentation molecules, including MHC class II. They play a crucial role in scavenging and presenting antigens to lymphocytes. Overall, the basement membrane is critical in regulating BBB permeability to cells (Galea, 2021).

Altogether, the results of the GSEA and subsequent observations regarding the involvement of immunological processes at the blood-brain barrier could support a role for BBB permeability and, consequently, tracer extraction in the observed phenomena.

5.2.2 Body weight and K_1 measures

The analyses indicated a significant inverse association between body weight and the K_1 parameter across all datasets and levels, except at the ROI level for Dataset 1. This effect could be partially attributed to alterations in cerebral blood flow, as elevated body mass index (BMI) is associated with reduced cerebral blood perfusion (Knight et al., 2021). Additionally, reduced

extraction may also play a role in this inverse association. Increased body mass and obesity have been linked to chronic peripheral inflammation (Forsythe et al., 2008; Murray et al., 2015; Visser et al., 1999). Therefore, the same mechanism that links elevated CRP to reduced K_1 could explain the inverse relationship between body mass measures and K_1. This is supported by the significant positive association between log(CRP) and body weight in Dataset 1 (see Section 4.4.1). Additionally, the partial alignment between the patterns showing the negative effect of weight and the negative effect of CRP levels on K_1 (see Section 4.4.2) suggests that the underlying mechanisms of these effects might partially overlap. The imaging transcriptomics analysis conducted on the maps representing the negative effect of body weight on K_1 could potentially help elucidate the underlying biological mechanisms driving this effect. However, for a comprehensive and insightful interpretation of the results from the gene set enrichment analysis, future clinical consultation will be necessary.

5.2.3 Gender differences in TSPO tracers influx

This work also revealed a significant effect of gender on the blood-to-brain influx rate of TSPO radiotracers across all three datasets and levels, with an increase observed in females compared to males. This effect is unlikely linked to extraction. Instead, it could be explained by the higher cerebral blood flow found in females, who exhibit an increase of around 15% compared to males (Aanerud et al., 2017; Mazzucco et al., 2024; Rodriguez et al., 1988). Given the magnitude of the increase observed in women in the present study (see Section 4.4.1), the variability could largely be attributed to differences in blood perfusion.

5.3 Implications of the findings

5.3.1 Support for a new model of peripheral-central immune interactions

The main finding of this work, represented by the negative association between the concentration of C-reactive protein (CRP) and the blood-to-brain influx rate of TSPO radiotracers, further supports the emerging model of peripheral-to-central immune interactions (Turkheimer et al., 2023). Indeed, if the potential reduction in BBB permeability affects more than just lipophilic molecules like TSPO radiotracers, it could strengthen the hypothesis that the permeability of a healthy BBB decreases in response to increased peripheral inflammation, as indicated by CRP levels. According to this theory, the elevation of circulating cytokines reduces blood-brain barrier permeability, disrupting homeostasis and causing mild sickness behavior. Subsequently, when persistent inflammation becomes chronic, structural changes in barrier function occur, leading to depressive behavior accompanied by activated microglia responding to prolonged

disturbances in solute concentrations and the blood-brain barrier (BBB). The persistent disturbance of homeostasis particularly affects neotenic regions, such as the prefrontal cortex, which retain high synaptic density in the adult brain and are consequently the most metabolically active (Petanjek et al., 2011). In the present study, both ROI-level and voxel-level analyses revealed that frontal regions are among those where the impact of peripheral inflammation on barrier permeability is most pronounced. These findings are especially valuable given that these areas are well known to be involved in mood regulation and depression (Goldin et al., 2008; Talbot & Cooper, 2006).

While this model originally applies to depressive patients with a mild grade of peripheral inflammation, the present study could potentially posit the effect theorized in this model as both a disease-agnostic and transdiagnostic effect across healthy and psychiatric populations. Future research could investigate the relation of barrier permeability with shared clinical symptoms among different neuropsychiatric cohorts. Additionally, further research is needed to deepen our understanding of the critical interplay between central and peripheral immunity. Recent findings have highlighted the role of skull bone marrow and venous sinuses in mediating immune interactions, showing significant associations between extra-axial inflammatory signals in the skull and parameningeal spaces and both central and peripheral immune activity in depression (Eiff et al., 2024).

5.3.2 Methodological considerations in TSPO quantification

The insights from the present work could shed light on several methodological issues encountered in TSPO quantification. Importantly, variations in the rate constant K_1 are reflected in the calculations of the volume of distribution and may be misinterpreted as changes in TSPO density. Changes in tracer blood-to-tissue transport have been shown to account for up to 77 % of the variation in V_T measures in [^{11}C]-PBR28 PET data (Nettis et al., 2020). Given that this study found variations in the K_1 rate due to differences in body mass, gender, and especially peripheral inflammatory status, these factors should be carefully considered when interpreting TSPO PET outcomes. This could explain the paradoxical and inconclusive results found in the context of schizophrenia, specifically when V_T was used as the representative outcome (Marques et al., 2019). Additionally, the findings from this work could elucidate the results of a [^{11}C]-PBR28 imaging study on healthy individuals (Tuisku et al., 2019). This study observed that V_T had a significant negative correlation with BMI and differed significantly between males and females, with women exhibiting a higher V_T (approximately 17% increase in total grey matter). Given the direct proportionality between K_1 and V_T, the observed effects of body weight and gender on the blood-to-brain influx rate of TSPO PET tracers could account for the discrepancies reported by Tuisku et al. (2019).

These findings underscore the importance of meticulously matching healthy and patient groups in cross-sectional TSPO studies with regard to body weight, gender, and potentially peripheral inflammatory status. In the context of psychiatric disorders, this can be challenging given the higher prevalence of males in the schizophrenic population (Jauhar et al., 2022) and the higher BMI of schizophrenic patients (Annamalai et al., 2017), particularly after antipsychotic treatment (Correll et al., 2011). This observation also applies to the major depressive disorder population, where weight gain is a known effect of antidepressant treatment (Gafoor et al., 2018). Additionally, it is worth noting that patients in both MDD and schizophrenia populations are generally associated with a status of peripheral inflammation (Na et al., 2014; Osimo et al., 2020; Osimo et al., 2019; Pitharouli et al., 2021).

5.4 Study limitations

From a methodological point of view the work exhibited some limitations, mainly linked to the extraction of the image-derived input function and the optimization of the time window for model fitting. The first, despite representing a crucial and necessary step to enable the blood-free estimation, is affected by the relatively low spatial and temporal resolution in PET dynamic data. This might have caused relevant partial volume effects and could have impaired the possibility of accurately following the fast rising and descending parts of the curve, thus introducing variable bias across subjects. Technological advancements in PET scanners would hopefully lead to a more reliable decription of IDIF (Volpi et al., 2023). In addition, the selection of the optimal time interval for model fitting was not trivial, specifically for the tracer $[^{11}C]$-PK11195, where the framework was applied for the first time. The absence of blood data from arterial sampling to assess the radiotracer's metabolism may have affected the first validation of the methodology.

Chapter 6

Conclusion

This study presents a significant advancement in the non-invasive quantification of TSPO PET radiotracer dynamics, applying a robust methodology for estimating the blood-to-brain influx rate constant (K_1) without the need for blood sampling. By validating this approach with the first-generation tracer [^{11}C]-PK11195 and extending it to the second-generation tracer [^{11}C]-PBR28, the methodology has demonstrated both versatility and reliability. The transition from region-of-interest (ROI) to voxel-level analysis has provided an invaluable tool for detailed mapping of the K_1 parameter, enhancing spatial resolution and enabling unique insights into brain TSPO tracers uptake.

Key findings include a consistent negative association between peripheral inflammation, as indicated by CRP levels, and K_1 across multiple datasets and neuropsychiatric conditions. Remarkably, the microparameter was unaffected by the psychiatric disease. These results support the emerging model of peripheral-to-central immune interaction and highlight the influence of peripheral inflammation on blood-brain barrier (BBB) permeability. Additionally, significant effects of body mass index and gender on K_1 underscore the necessity of controlling for these variables and peripheral inflammatory status in TSPO PET studies to avoid misinterpretation of TSPO density measures.

This work not only supports new insights into the mechanisms of neuroinflammation and its relationship with peripheral immune markers but also addresses critical methodological challenges in TSPO PET quantification. The findings suggest a potential transdiagnostic effect of peripheral inflammation on brain function and emphasize the need for careful consideration of demographic and physiological variables in future neuroimaging studies. The development of this non-invasive, blood-free methodology paves the way for more accessible and comprehensive investigations into neuroinflammatory processes and their implications for various brain disorders.

Bibliography

Aanerud, J., Borghammer, P., Rodell, A., Jónsdottir, K. Y., & Gjedde, A. (2017). Sex differences of human cortical blood flow and energy metabolism. *Journal of Cerebral Blood Flow and Metabolism*, *37*. https://doi.org/10.1177/0271678X16668536

Aguilar-Valles, A., Rodrigue, B., & Matta-Camacho, E. (2020). Maternal immune activation and the development of dopaminergic neurotransmission of the offspring: Relevance for schizophrenia and other psychoses. *Frontiers in Psychiatry*, *11*. https://doi.org/10.3389/fpsyt.2020.00852

Aloisi, F., Ria, F., Columba-Cabezas, S., Hess, H., Penna, G., & Adorini, L. (1999). Relative efficiency of microglia, astrocytes, dendritic cells and b cells in naive cd4+ t cell priming and th1/th2 cell restimulation. *European Journal of Immunology*, *29*. https://doi.org/10.1002/(sici)1521-4141(199909)29:09<2705::aid-immu2705>3.0.co;2-1

Annamalai, A., Kosir, U., & Tek, C. (2017). Prevalence of obesity and diabetes in patients with schizophrenia. *World Journal of Diabetes*, *8*. https://doi.org/10.4239/wjd.v8.i8.390

Bagchi, S., Chhibber, T., Lahooti, B., Verma, A., Borse, V., & Jayant, R. D. (2019). In-vitro blood-brain barrier models for drug screening and permeation studies: An overview. https://doi.org/10.2147/DDDT.S218708

Benros, M. E., Nielsen, P. R., Nordentoft, M., Eaton, W. W., Dalton, S. O., & Mortensen, P. B. (2011). Autoimmune diseases and severe infections as risk factors for schizophrenia: A 30-year population-based register study. *American Journal of Psychiatry*, *168*. https://doi.org/10.1176/appi.ajp.2011.11030516

Bertoldo, A., Rizzo, G., & Veronese, M. (2014). Deriving physiological information from PET images: From SUV to compartmental modelling. *Clinical and Translational Imaging*, *2*. https://doi.org/10.1007/s40336-014-0067-x

Bloomfield, P. S., Selvaraj, S., Veronese, M., Rizzo, G., Bertoldo, A., Owen, D. R., Bloomfield, M. A., Bonoldi, I., Kalk, N., Turkheimer, F., McGuire, P., de Paola, V., & Howes, O. D. (2016). Microglial activity in people at ultra high risk of psychosis and in schizophrenia: An [11 C]PBR28 PET brain imaging study. *American Journal of Psychiatry*, *173*, 44–52. https://doi.org/10.1176/appi.ajp.2015.14101358

Bullmore, E. (2018). *The inflamed mind: A radical new approach to depression*. Picador.

Carson, R. (1993). PET parameter estimation using linear integration methods: Bias and variability considerations. *Quantification of brain function: tracer kinetics and image analysis in brain PET*, 499–507.

Chamberlain, S. R., Cavanagh, J., Boer, P. D., Mondelli, V., Jones, D. N., Drevets, W. C., Cowen, P. J., Harrison, N. A., Pointon, L., Pariante, C. M., & Bullmore, E. T. (2019). Treatment-resistant depression and peripheral C-reactive protein. *British Journal of Psychiatry*, *214*. https://doi.org/10.1192/bjp.2018.66

Chauveau, F., Boutin, H., Camp, N. V., Dollé, F., & Tavitian, B. (2008). Nuclear imaging of neuroinflammation: A comprehensive review of [11C]PK11195 challengers. *European Journal of Nuclear Medicine and Molecular Imaging*, *35*, 2304–2319. https://doi.org/10.1007/s00259-008-0908-9

Cherry, S. R., Sorenson, J. A., & Phelps, M. E. (2012). Chapter 21 - tracer kinetic modeling. In S. R. Cherry, J. A. Sorenson, & M. E. Phelps (Eds.), *Physics in nuclear medicine (fourth edition)* (Fourth Edition, pp. 379–405). W.B. Saunders. https://doi.org/https://doi.org/10.1016/B978-1-4160-5198-5.00021-6

Choi, Y.-K., & Kim, K.-W. (2008). Blood-neural barrier: Its diversity and coordinated cell-to-cell communication. *BMB Reports*, *41*, 345–352. https://doi.org/10.5483/BMBRep.2008.41.5.345

Cobelli, C., Finkelstein, L., & Carson, E. R. (1982). Mathematical modelling of endocrine and metabolic systems: Model formulation, identification and validation. *Mathematics and Computers in Simulation*, *24*. https://doi.org/10.1016/0378-4754(82)90641-3

Cornell, J., Salinas, S., Huang, H. Y., & Zhou, M. (2022). Microglia regulation of synaptic plasticity and learning and memory. *Neural Regeneration Research*, *17*. https://doi.org/10.4103/1673-5374.322423

Correll, C. U., Lencz, T., & Malhotra, A. K. (2011). Antipsychotic drugs and obesity. *Trends in Molecular Medicine*, *17*. https://doi.org/10.1016/j.molmed.2010.10.010

Coura-Filho, G. B., Torres Silva de Oliveira, M., & Morais de Campos, A. L. (2022). Basic principles of positron emission tomography. In *Nuclear medicine in endocrine disorders: Diagnosis and therapy* (pp. 15–20). Springer International Publishing. https://doi.org/10.1007/978-3-031-13224-7_3

Dahoun, T., Calcia, M. A., Veronese, M., Bloomfield, P., Marques, T. R., Turkheimer, F., & Howes, O. D. (2019). The association of psychosocial risk factors for mental health with a brain marker altered by inflammation: A translocator protein (TSPO) PET imaging study. *Brain, Behavior, and Immunity*, *80*. https://doi.org/10.1016/j.bbi.2019.05.023

DiSabato, D. J., Quan, N., & Godbout, J. P. (2016). Neuroinflammation: The devil is in the details. *Journal of Neurochemistry*, *139*, 136–153. https://doi.org/10.1111/jnc.13607

Eiff, B., Bullmore, E. T., Clatworthy, M. R., Fryer, T. D., Pariante, C. M., Mondelli, V., Maccioni, L., Hadjikhani, N., Loggia, M. L., Moskowitz, M. A., et al. (2024). Extra-axial inflammatory signal and its relation to peripheral and central immunity in depression. *medRxiv*. https://doi.org/10.1101/2024.03.15.24304342

Everett, B. A., Oquendo, M. A., Abi-Dargham, A., Nobler, M. S., Devanand, D. P., Lisanby, S. H., Mann, J. J., & Parsey, R. V. (2009). Safety of radial arterial catheterization in PET research subjects. *Journal of Nuclear Medicine*, *50*. https://doi.org/10.2967/jnumed.109.063206

Forsythe, L. K., Wallace, J. M., & Livingstone, M. B. E. (2008). Obesity and inflammation: The effects of weight loss. *Nutrition Research Reviews*, *21*. https://doi.org/10.1017/S0954422408138732

Fung, E. K., Planeta-Wilson, B., Mulnix, T., & Carson, R. E. (2009). A multimodal approach to image-derived input functions for brain PET. *IEEE Nuclear Science Symposium Conference Record*. https://doi.org/10.1109/NSSMIC.2009.5401977

Gafoor, R., Booth, H. P., & Gulliford, M. C. (2018). Antidepressant utilisation and incidence of weight gain during 10 years' follow-up: Population based cohort study. *BMJ (Online)*, *361*. https://doi.org/10.1136/bmj.k1951

Galea, I. (2021). The blood–brain barrier in systemic infection and inflammation. *Cellular and Molecular Immunology*, *18*. https://doi.org/10.1038/s41423-021-00757-x

Galea, I., Bernardes-Silva, M., Forse, P. A., Rooijen, N. V., Liblau, R. S., & Perry, V. H. (2007). An antigen-specific pathway for cd8 t cells across the blood-brain barrier. *Journal of Experimental Medicine*, *204*. https://doi.org/10.1084/jem.20070064

Giacomel, A., Martins, D., Frigo, M., Turkheimer, F., Williams, S. C., Dipasquale, O., & Veronese, M. (2022). Integrating neuroimaging and gene expression data using the imaging transcriptomics toolbox. *STAR Protocols*, *3*. https://doi.org/10.1016/j.xpro.2022.101315

Gimsa, U., Mitchison, N. A., & Brunner-Weinzierl, M. C. (2013). Immune privilege as an intrinsic cns property: Astrocytes protect the cns against t-cell-mediated neuroinflammation. *Mediators of Inflammation*, *2013*. https://doi.org/10.1155/2013/320519

Goldin, P. R., McRae, K., Ramel, W., & Gross, J. J. (2008). The neural bases of emotion regulation: Reappraisal and suppression of negative emotion. *Biological Psychiatry*, *63*. https://doi.org/10.1016/j.biopsych.2007.05.031

Hannestad, J., Subramanyam, K., DellaGioia, N., Planeta-Wilson, B., Weinzimmer, D., Pittman, B., & Carson, R. E. (2012). Glucose metabolism in the insula and cingulate is affected

by systemic inflammation in humans. *Journal of Nuclear Medicine*, *53*. https://doi.org/10.2967/jnumed.111.097014

Harrison, N. A., Brydon, L., Walker, C., Gray, M. A., Steptoe, A., & Critchley, H. D. (2009). Inflammation causes mood changes through alterations in subgenual cingulate activity and mesolimbic connectivity. *Biological Psychiatry*, *66*. https://doi.org/10.1016/j.biopsych.2009.03.015

Haruwaka, K., Ikegami, A., Tachibana, Y., Ohno, N., Konishi, H., Hashimoto, A., Matsumoto, M., Kato, D., Ono, R., Kiyama, H., Moorhouse, A. J., Nabekura, J., & Wake, H. (2019). Dual microglia effects on blood brain barrier permeability induced by systemic inflammation. *Nature Communications*, *10*. https://doi.org/10.1038/s41467-019-13812-z

Hawkins, B. T., & Davis, T. P. (2005). The blood-brain barrier/neurovascular unit in health and disease. *Pharmacological Reviews*, *57*. https://doi.org/10.1124/pr.57.2.4

Heneka, M. T., Carson, M. J., Khoury, J. E., Landreth, G. E., Brosseron, F., Feinstein, D. L., Jacobs, A. H., Wyss-Coray, T., Vitorica, J., Ransohoff, R. M., Herrup, K., Frautschy, S. A., Finsen, B., Brown, G. C., Verkhratsky, A., Yamanaka, K., Koistinaho, J., Latz, E., Halle, A., … Kummer, M. P. (2015). Neuroinflammation in alzheimer's disease. *The Lancet Neurology*, *14*, 388–405. https://doi.org/10.1016/S1474-4422(15)70016-5

Holmes, S. E., Hinz, R., Conen, S., Gregory, C. J., Matthews, J. C., Anton-Rodriguez, J. M., Gerhard, A., & Talbot, P. S. (2018). Elevated translocator protein in anterior cingulate in major depression and a role for inflammation in suicidal thinking: A positron emission tomography study. *Biological Psychiatry*, *83*. https://doi.org/10.1016/j.biopsych.2017.08.005

Jauhar, S., Johnstone, M., & McKenna, P. J. (2022). Schizophrenia. *The Lancet*, *399*(10323), 473–486. https://doi.org/https://doi.org/10.1016/S0140-6736(21)01730-X

Jučaite, A., Cselényi, Z., Arvidsson, A., Åhlberg, G., Julin, P., Varnäs, K., Stenkrona, P., Andersson, J., Halldin, C., & Farde, L. (2012). Kinetic analysis and test-retest variability of the radioligand [11C]R-PK11195 binding to TSPO in the human brain - a PET study in control subjects. *EJNMMI Research*, *2*. https://doi.org/10.1186/2191-219X-2-15

Kadry, H., Noorani, B., & Cucullo, L. (2020). A blood–brain barrier overview on structure, function, impairment, and biomarkers of integrity. *Fluids and Barriers of the CNS*, *17*. https://doi.org/10.1186/s12987-020-00230-3

Kim, E. J., & Yu, S. W. (2015). Translocator protein 18 kDa (TSPO): Old dogma, new mice, new structure, and new questions for neuroprotection. *Neural Regeneration Research*, *10*. https://doi.org/10.4103/1673-5374.158338

Knight, S. P., Laird, E., Williamson, W., O'Connor, J., Newman, L., Carey, D., Looze, C. D., Fagan, A. J., Chappell, M. A., Meaney, J. F., & Kenny, R. A. (2021). Obesity is associ-

ated with reduced cerebral blood flow – modified by physical activity. *Neurobiology of Aging*, *105*, 35–47. https://doi.org/10.1016/J.NEUROBIOLAGING.2021.04.008

Kotasidis, F. A., Tsoumpas, C., & Rahmim, A. (2014). Advanced kinetic modelling strategies: Towards adoption in clinical PET imaging. https://doi.org/10.1007/s40336-014-0069-8

Kreutzberg, G. W. (1996). Microglia: A sensor for pathological events in the cns. *Trends in Neurosciences*, *19*. https://doi.org/10.1016/0166-2236(96)10049-7

Kwon, H. S., & Koh, S. H. (2020). Neuroinflammation in neurodegenerative disorders: The roles of microglia and astrocytes. *Translational Neurodegeneration*, *9*. https://doi.org/10.1186/s40035-020-00221-2

Lake, B. B., Chen, S., Sos, B. C., Fan, J., Kaeser, G. E., Yung, Y. C., Duong, T. E., Gao, D., Chun, J., Kharchenko, P. V., & Zhang, K. (2018). Integrative single-cell analysis of transcriptional and epigenetic states in the human adult brain. *Nature Biotechnology*, *36*. https://doi.org/10.1038/nbt.4038

Lee, Y., Park, Y., Nam, H., Lee, J. W., & Yu, S. W. (2020). Translocator protein (TSPO): The new story of the old protein in neuroinflammation. *BMB Reports*, *53*. https://doi.org/10.5483/BMBRep.2020.53.1.273

Li, H., Sagar, A. P., & Kéri, S. (2018). Translocator protein (18 kDa TSPO) binding, a marker of microglia, is reduced in major depression during cognitive-behavioral therapy. *Progress in Neuro-Psychopharmacology and Biological Psychiatry*, *83*. https://doi.org/10.1016/j.pnpbp.2017.12.011

Maccioni, L., Carranza Mellana, M., Brusaferri, L., Silvestri, E., Bertoldo, A., Schubert, J. J., Nettis, M. A., Mondelli, V., Howes, O., Turkheimer, F. E., Bottlaender, M., Bodini, B., Stankoff, B., Loggia, M. L., & Veronese, M. (2024). A blood-free modeling approach for the quantification of the blood-to-brain tracer exchange in TSPO PET imaging. *Frontiers in Neuroscience*, *18*. https://doi.org/10.3389/fnins.2024.1395769

Marques, T. R., Ashok, A. H., Pillinger, T., Veronese, M., Turkheimer, F. E., Dazzan, P., Sommer, I. E., & Howes, O. D. (2019). Neuroinflammation in schizophrenia: Meta-analysis of in vivo microglial imaging studies. *Psychological Medicine*, *49*. https://doi.org/10.1017/S0033291718003057

Marques, T. R., Veronese, M., Owen, D. R., Rabiner, E. A., Searle, G. E., & Howes, O. D. (2021). Specific and non-specific binding of a tracer for the translocator-specific protein in schizophrenia: An [11C]-PBR28 blocking study. *European Journal of Nuclear Medicine and Molecular Imaging*, *48*. https://doi.org/10.1007/s00259-021-05327-x

Martins, D., Giacomel, A., Williams, S. C., Turkheimer, F., Dipasquale, O., Veronese, M., Batzu, L., Bertoldo, A., Bullmore, E., Cecchin, D., Chaudhuri, R., Corbetta, M., Dunn, J., Farrel, C., Forsberg, A., Fujita, M., Hammers, A., Innis, R., Kosek, E., … Zanotti-

Fregonar, P. (2021). Imaging transcriptomics: Convergent cellular, transcriptomic, and molecular neuroimaging signatures in the healthy adult human brain. *Cell Reports*, *37*. https://doi.org/10.1016/j.celrep.2021.110173

Mato, M., Ookawara, S., Sakamoto, A., Aikawa, E., Ogawa, T., Mitsuhashi, U., Masuzawa, T., Suzuki, H., Honda, M., Yazaki, Y., Watanabe, E., Luoma, J., Yla-Herttuala, S., Fraser, I., Gordon, S., & Kodama, T. (1996). Involvement of specific macrophage-lineage cells surrounding arterioles in barrier and scavenger function in brain cortex. *Proceedings of the National Academy of Sciences of the United States of America*, *93*. https://doi.org/10.1073/pnas.93.8.3269

Mazzucco, S., Li, L., Tuna, M. A., & Rothwell, P. M. (2024). Age-specific sex-differences in cerebral blood flow velocity in relation to haemoglobin levels. *European Stroke Journal*, 23969873241245631. https://doi.org/10.1177/23969873241245631

Mintun, M. A., Raichle, M. E., Kilbourn, M. R., Wooten, G. F., & Welch, M. J. (1984). A quantitative model for the in vivo assessment of drug binding sites with positron emission tomography. *Annals of Neurology*, *15*. https://doi.org/10.1002/ana.410150302

Mourik, J. E., Lubberink, M., Klumpers, U. M., Comans, E. F., Lammertsma, A. A., & Boellaard, R. (2008). Partial volume corrected image derived input functions for dynamic PET brain studies: Methodology and validation for [11C]flumazenil. *NeuroImage*, *39*. https://doi.org/10.1016/j.neuroimage.2007.10.022

Murray, E. T., Hardy, R., Hughes, A., Wills, A., Sattar, N., Deanfield, J., Kuh, D., & Whincup, P. (2015). Overweight across the life course and adipokines, inflammatory and endothelial markers at age 60-64 years: Evidence from the 1946 birth cohort. *International Journal of Obesity*, *39*. https://doi.org/10.1038/ijo.2015.19

Na, K. S., Jung, H. Y., & Kim, Y. K. (2014). The role of pro-inflammatory cytokines in the neuroinflammation and neurogenesis of schizophrenia. *Progress in Neuro-Psychopharmacology and Biological Psychiatry*, *48*. https://doi.org/10.1016/j.pnpbp.2012.10.022

Nettis, M. A., Veronese, M., Nikkheslat, N., Mariani, N., Lombardo, G., Sforzini, L., Enache, D., Harrison, N. A., Turkheimer, F. E., Mondelli, V., & Pariante, C. M. (2020). PET imaging shows no changes in TSPO brain density after IFN-α immune challenge in healthy human volunteers. *Translational Psychiatry*, *10*. https://doi.org/10.1038/s41398-020-0768-z

Nguyen, T. T., Nguyen, T. T. D., Vo, T. K., Tran, N. M. A., Nguyen, M. K., Vo, T. V., & Vo, G. V. (2021). Nanotechnology-based drug delivery for central nervous system disorders. *Biomedicine and Pharmacotherapy*, *143*. https://doi.org/10.1016/j.biopha.2021.112117

Nimmerjahn, A., Kirchhoff, F., & Helmchen, F. (2005). Neuroscience: Resting microglial cells are highly dynamic surveillants of brain parenchyma in vivo. *Science*, *308*. https://doi.org/10.1126/science.1110647

Osimo, E. F., Pillinger, T., Rodriguez, I. M., Khandaker, G. M., Pariante, C. M., & Howes, O. D. (2020). Inflammatory markers in depression: A meta-analysis of mean differences and variability in 5,166 patients and 5,083 controls. *Brain, Behavior, and Immunity*, *87*. https://doi.org/10.1016/j.bbi.2020.02.010

Osimo, E. F., Baxter, L. J., Lewis, G., Jones, P. B., & Khandaker, G. M. (2019). Prevalence of low-grade inflammation in depression: A systematic review and meta-analysis of CRP levels. *Psychological Medicine*, *49*. https://doi.org/10.1017/S0033291719001454

Parsey, R. V., Slifstein, M., Hwang, D. R., Abi-Dargham, A., Simpson, N., Mawlawi, O., Guo, N. N., Heertum, R. V., Mann, J. J., & Laruelle, M. (2000). Validation and reproducibility of measurement of 5-ht(1a) receptor parameters with [carbonyl-11 C]way-100635 in humans: Comparison of arterial and reference tissue input functions. *Journal of Cerebral Blood Flow and Metabolism*, *20*. https://doi.org/10.1097/00004647-200007000-00011

Petanjek, Z., Judaš, M., Šimić, G., Rašin, M. R., Uylings, H. B., Rakic, P., & Kostović, I. (2011). Extraordinary neoteny of synaptic spines in the human prefrontal cortex. *Proceedings of the National Academy of Sciences of the United States of America*, *108*. https://doi.org/10.1073/pnas.1105108108

Peters van Ton, A. M., Leijte, G. P., Franssen, G. M., Bruse, N., Booij, J., Doorduin, J., Rijpkema, M., Kox, M., Abdo, W. F., & Pickkers, P. (2021). Human in vivo neuroimaging to detect reprogramming of the cerebral immune response following repeated systemic inflammation. *Brain, Behavior, and Immunity*, *95*. https://doi.org/10.1016/j.bbi.2021.04.004

Pitharouli, M. C., Hagenaars, S. P., Glanville, K. P., Coleman, J. R., Hotopf, M., Lewis, C. M., & Pariante, C. M. (2021). Elevated C-reactive protein in patients with depression, independent of genetic, health, and psychosocial factors: Results from the uk biobank. *American Journal of Psychiatry*, *178*. https://doi.org/10.1176/appi.ajp.2020.20060947

Plavén-Sigray, P., & Cervenka, S. (2019). Meta-analytic studies of the glial cell marker TSPO in psychosis - a question of apples and pears? *Psychological Medicine*, *49*. https://doi.org/10.1017/S003329171800421X

Renkin, E. M. (1959). Transport of potassium-42 from blood to tissue in isolated mammalian skeletal muscles. *The American journal of physiology*, *197*. https://doi.org/10.1152/ajplegacy.1959.197.6.1205

Richards, E. M., Zanotti-Fregonara, P., Fujita, M., Newman, L., Farmer, C., Ballard, E. D., Machado-Vieira, R., Yuan, P., Niciu, M. J., Lyoo, C. H., Henter, I. D., Salvadore, G.,

Drevets, W. C., Kolb, H., Innis, R. B., & Zarate, C. A. (2018). PET radioligand binding to translocator protein (TSPO) is increased in unmedicated depressed subjects. *EJNMMI Research*, *8*. https://doi.org/10.1186/s13550-018-0401-9

Rodriguez, G., Warkentin, S., Risberg, J., & Rosadini, G. (1988). Sex differences in regional cerebral blood flow. *Journal of Cerebral Blood Flow and Metabolism*, *8*. https://doi.org/10.1038/jcbfm.1988.133

Rush, A. J., Trivedi, M. H., Wisniewski, S. R., Nierenberg, A. A., Stewart, J. W., Warden, D., Niederehe, G., Thase, M. E., Lavori, P. W., Lebowitz, B. D., McGrath, P. J., Rosenbaum, J. F., Sackeim, H. A., Kupfer, D. J., Luther, J., & Fava, M. (2006). Acute and longer-term outcomes in depressed outpatients requiring one or several treatment steps: A star*d report. *American Journal of Psychiatry*, *163*. https://doi.org/10.1176/ajp.2006.163.11.1905

Schubert, J., Tonietto, M., Turkheimer, F., Zanotti-Fregonara, P., & Veronese, M. (2021). Supervised clustering for TSPO PET imaging. *European Journal of Nuclear Medicine and Molecular Imaging*, *49*. https://doi.org/10.1007/s00259-021-05309-z

Schubert, J. J., Veronese, M., Fryer, T. D., Manavaki, R., Kitzbichler, M. G., Nettis, M. A., Mondelli, V., Pariante, C. M., Bullmore, E. T., Turkheimer, F. E., Wlazly, D., Dickinson, A., Foster, A., Knight, C., Leckey, C., Morgan, P., Morgan, A., O'Hagan, C., Touchard, S., … Mount, H. (2021). A modest increase in 11C-PK11195-positron emission tomography TSPO binding in depression is not associated with serum C-reactive protein or body mass index. *Biological Psychiatry: Cognitive Neuroscience and Neuroimaging*, *6*, 716–724. https://doi.org/10.1016/j.bpsc.2020.12.017

Setiawan, E., Attwells, S., Wilson, A. A., Mizrahi, R., Rusjan, P. M., Miler, L., Xu, C., Sharma, S., Kish, S., Houle, S., & Meyer, J. H. (2018). Association of translocator protein total distribution volume with duration of untreated major depressive disorder: A cross-sectional study. *The Lancet Psychiatry*, *5*. https://doi.org/10.1016/S2215-0366(18)30048-8

Setiawan, E., Wilson, A. A., Mizrahi, R., Rusjan, P. M., Miler, L., Rajkowska, G., Suridjan, I., Kennedy, J. L., Rekkas, P. V., Houle, S., & Meyer, J. H. (2015). Role of translocator protein density, a marker of neuroinflammation, in the brain during major depressive episodes. *JAMA Psychiatry*, *72*. https://doi.org/10.1001/jamapsychiatry.2014.2427

Smith, S. M., & Nichols, T. E. (2009). Threshold-free cluster enhancement: Addressing problems of smoothing, threshold dependence and localisation in cluster inference. *NeuroImage*, *44*. https://doi.org/10.1016/j.neuroimage.2008.03.061

Souza, A. M. D., Pitombeira, M. S., Souza, L. E. D., Marques, F. L. N., Buchpiguel, C. A., Real, C. C., & Faria, D. D. P. (2021). 11C-PK11195 plasma metabolization has the same

rate in multiple sclerosis patients and healthy controls: A cross-sectional study. *Neural Regeneration Research*, *16*. https://doi.org/10.4103/1673-5374.313062

Spampinato, S. F., Costantino, G., Merlo, S., Canonico, P. L., & Sortino, M. A. (2022). Microglia contributes to baf-312 effects on blood–brain barrier stability. *Biomolecules*, *12*. https://doi.org/10.3390/biom12091174

Stępnicki, P., Kondej, M., & Kaczor, A. A. (2018). Current concepts and treatments of schizophrenia. *Molecules*, *23*, 2087. https://doi.org/10.3390/molecules23082087

Subramanian, A., Tamayo, P., Mootha, V. K., Mukherjee, S., Ebert, B. L., Gillette, M. A., Paulovich, A., Pomeroy, S. L., Golub, T. R., Lander, E. S., & Mesirov, J. P. (2005). Gene set enrichment analysis: A knowledge-based approach for interpreting genome-wide expression profiles. *Proceedings of the National Academy of Sciences of the United States of America*, *102*. https://doi.org/10.1073/pnas.0506580102

Suo, Q., Deng, L., Chen, T., Wu, S., Qi, L., Liu, Z., He, T., Tian, H. L., Li, W., Tang, Y., Yang, G. Y., & Zhang, Z. (2023). Optogenetic activation of astrocytes reduces blood-brain barrier disruption via il-10 in stroke. *Aging and Disease*, *14*. https://doi.org/10.14336/AD.2023.0226

Tai, Y. F., & Piccini, P. (2004). Applications of positron emission tomography (PET) in neurology. *Journal of Neurology, Neurosurgery and Psychiatry*, *75*. https://doi.org/10.1136/jnnp.2003.028175

Talbot, P. S., & Cooper, S. J. (2006). Anterior cingulate and subgenual prefrontal blood flow changes following tryptophan depletion in healthy males. *Neuropsychopharmacology*, *31*. https://doi.org/10.1038/sj.npp.1301022

Tonietto, M., Rizzo, G., Veronese, M., Fujita, M., Zoghbi, S. S., Zanotti-Fregonara, P., & Bertoldo, A. (2016). Plasma radiometabolite correction in dynamic PET studies: Insights on the available modeling approaches. https://doi.org/10.1177/0271678X15610585

Tuisku, J., Plavén-Sigray, P., Gaiser, E. C., Airas, L., Al-Abdulrasul, H., Brück, A., Carson, R. E., Chen, M. K., Cosgrove, K. P., Ekblad, L., Esterlis, I., Farde, L., Forsberg, A., Halldin, C., Helin, S., Kosek, E., Lekander, M., Lindgren, N., Marjamäki, P., … Cervenka, S. (2019). Effects of age, BMI and sex on the glial cell marker TSPO — a multicentre [11C]PBR28 hrrt PET study. *European Journal of Nuclear Medicine and Molecular Imaging*, *46*. https://doi.org/10.1007/s00259-019-04403-7

Turkheimer, F. E., Althubaity, N., Schubert, J., Nettis, M. A., Cousins, O., Dima, D., Mondelli, V., Bullmore, E. T., Pariante, C., & Veronese, M. (2021). Increased serum peripheral C-reactive protein is associated with reduced brain barriers permeability of TSPO radioligands in healthy volunteers and depressed patients: Implications for inflammation

and depression. *Brain, Behavior, and Immunity*, *91*, 487–497. https://doi.org/10.1016/j.bbi.2020.10.025

Turkheimer, F. E., Edison, P., Pavese, N., Roncaroli, F., Anderson, A. N., Hammers, A., Gerhard, A., Hinz, R., Tai, Y. F., & Brooks, D. J. (2007). Reference and target region modeling of [11C]-R-PK11195 brain studies. *Journal of Nuclear Medicine*, *48*. https://jnm.snmjournals.org/content/48/1/158

Turkheimer, F. E., Rizzo, G., Bloomfield, P. S., Howes, O., Zanotti-Fregonara, P., Bertoldo, A., & Veronese, M. (2015). The methodology of TSPO imaging with positron emission tomography. *Biochemical Society Transactions*, *43*. https://doi.org/10.1042/BST20150058

Turkheimer, F. E., Veronese, M., Mondelli, V., Cash, D., & Pariante, C. M. (2023). Sickness behaviour and depression: An updated model of peripheral-central immunity interactions. *Brain, Behavior, and Immunity*, *111*, 202–210. https://doi.org/10.1016/j.bbi.2023.03.031

Tziortzi, A. C., Searle, G. E., Tzimopoulou, S., Salinas, C., Beaver, J. D., Jenkinson, M., Laruelle, M., Rabiner, E. A., & Gunn, R. N. (2011). Imaging dopamine receptors in humans with [11C]-(+)-PHNO: Dissection of D3 signal and anatomy. *NeuroImage*, *54*. https://doi.org/10.1016/j.neuroimage.2010.06.044

Veronese, M., Marques, T. R., Bloomfield, P. S., Rizzo, G., Singh, N., Jones, D., Agushi, E., Mosses, D., Bertoldo, A., Howes, O., Roncaroli, F., & Turkheimer, F. E. (2018). Kinetic modelling of [11 C]PBR28 for 18 kDa translocator protein PET data: A validation study of vascular modelling in the brain using xbd173 and tissue analysis. *Journal of Cerebral Blood Flow and Metabolism*, *38*. https://doi.org/10.1177/0271678X17712388

Visser, M., Bouter, L. M., McQuillan, G. M., Wener, M. H., & Harris, T. B. (1999). Elevated C-reactive protein levels in overweight and obese adults. *Journal of the American Medical Association*, *282*. https://doi.org/10.1001/jama.282.22.2131

Volpi, T., Maccioni, L., Colpo, M., Debiasi, G., Capotosti, A., Ciceri, T., Carson, R. E., DeLorenzo, C., Hahn, A., Knudsen, G. M., Lammertsma, A. A., Price, J. C., Sossi, V., Wang, G., Zanotti-Fregonara, P., Bertoldo, A., & Veronese, M. (2023). An update on the use of image-derived input functions for human PET studies: New hopes or old illusions? *EJNMMI Research*, *13*. https://doi.org/10.1186/s13550-023-01050-w

WHO. (2021). *Depression* (Fact sheet). World Health Organization. https://www.who.int/news-room/fact-sheets/detail/depression

Yong, V. W. (2022). Microglia in multiple sclerosis: Protectors turn destroyers. *Neuron*, *110*, 3534–3548. https://doi.org/10.1016/j.neuron.2022.06.023

Zanotti-Fregonara, P., Chen, K., Liow, J. S., Fujita, M., & Innis, R. B. (2011). Image-derived input function for brain PET studies: Many challenges and few opportunities. *Journal of Cerebral Blood Flow and Metabolism*, *31*. https://doi.org/10.1038/jcbfm.2011.107

Acknowledgments

I would like to express my sincere gratitude to my supervisor, Prof. Mattia Veronese, for providing me with the opportunity to work in this fascinating research field and for his invaluable and continuous support. Special thanks are due to my co-supervisor, Lucia Maccioni, whose exceptional dedication guided me throughout this journey. I am deeply grateful to Manuela Moretto for her outstanding training and support in analyzing parametric maps. Additionally, I extend my thanks to Alessio Giacomel for the unique opportunity to work with his imaging transcriptomics toolbox.

I am also thankful to King's College London for supplying the data necessary for this study, and to all the participants who generously contributed their time and effort to advance research and science.

I am profoundly grateful to my parents, Novella and Claudio, who have always supported me unconditionally and nurtured my personal growth. I dedicate this thesis to them, my guiding lights in the storm.

I would like to thank all the members of my family and friends for their unwavering belief in me.

Finally, a special mention goes to my grandparents, Gemma and Lino. Although they are not here to witness my achievements, I am confident they would be proud of me.